Sparse Convolutional Beamforming for Ultrasound Imaging

Regev Cohen, *Graduate Student Member, IEEE*, and Yonina C. Eldar, *Fellow, IEEE*

Abstract— The standard technique used by commercial medical ultrasound systems to form B-mode images is delay and sum (DAS) beamforming. However, DAS often results in limited image resolution and contrast that are governed by the center frequency and the aperture size of the ultrasound transducer. A large number of elements lead to improved resolution but at the same time increase the data size and the system cost due to the receive electronics required for each element. Therefore, reducing the number of receiving channels while producing high-quality images is of great importance. In this paper, we introduce a nonlinear beamformer called COnvolutional Beamforming Algorithm (COBA), which achieves significant improvement of lateral resolution and contrast. In addition, it can be implemented efficiently using the fast Fourier transform. Based on the COBA concept, we next present two sparse beamformers with closed-form expressions for the sensor locations, which result in the same beam pattern as DAS and COBA while using far fewer array elements. Optimization of the number of elements shows that they require a minimal number of elements that are on the order of the square root of the number used by DAS. The performance of the proposed methods is tested and validated using simulated data, phantom scans, and *in vivo* cardiac data. The results demonstrate that COBA outperforms DAS in terms of resolution and contrast and that the suggested beamformers offer a sizable element reduction while generating images with an equivalent or improved quality in comparison with DAS.

Index Terms— Array processing, beam pattern, beamforming, contrast resolution, medical ultrasound, sparse arrays.

I. INTRODUCTION

ULTRASOUND imaging is one of the most common medical imaging modalities, allowing for noninvasive investigation of anatomical structures and blood flow. Cardiac, abdominal, fetal, and breast imaging are some of the applications where it is extensively used as a diagnostic tool.

In a conventional scanning process, short acoustic pulses are transmitted along a narrow beam from an array of transducer elements. During their propagation, echoes are scattered by acoustic impedance perturbations in the tissue and detected by the array elements. The backscattered radio-frequency (RF) signals are then processed in a way referred to as beamforming to create a line in the image. The beamformer is designed to focus and steer the ultrasound transducer toward a desired direction or point in space. The main goal of the beamformer is to generate a beam pattern with a narrow main lobe and low sidelobes [1]. The beam main-lobe width dictates the system resolution, while the sidelobe level controls the contrast so that the beam properties have a great impact on image quality [2].

In medical ultrasound imaging, the standard beamformer is delay and sum (DAS) [1], [3], which consists of delaying and weighting the reflected echoes before summing them. While its simplicity and real-time capabilities make DAS widely used in ultrasound scanners, it exhibits limited imaging resolution and contrast [4]. Increasing the number of elements, while keeping the array pitch below half a wavelength to avoid grating lobes [5], results in enhanced resolution. However, this increases channel data size and the system cost due to the receive electronics required for each element. Therefore, reducing the number of receiving channels while producing high-quality images is of great importance.

A. Related Work

Considering a full array, several methods to improve image quality have been proposed. Adaptive beamformers improve resolution without sacrificing contrast by dynamically changing the receive aperture weights based on the received data statistics [6]. The most common is Capon/minimum variance (MV) beamforming [7], which offers better contrast and resolution than DAS. However, its real time application is difficult due to the calculation of a covariance matrix and its inverse at each time instant. Its application to ultrasound imaging was studied extensively over the last decade, and many improved versions of MV with reduced complexity have been proposed [8]–[11]. Nilsen and Hafizovic [12] suggest a beamspace adaptive beamformer, BS-Capon, based on orthogonal beams formed in different directions. Jensen and Austeng [13] developed an adaptive beamformer called multibeam Capon that is based on multibeam covariance matrices. Using similar concepts, Jensen and Austeng [14] proposed a method called iterative adaptive approach [15].

Other related techniques have been presented such as applying various finite impulse response filters on each receive channel, instead of single apodization weights [16]. Chernyakova *et al.* [64] proposed a beamformer called iterative maximum-*a-posteriori* (iMAP) where both the interference and the signal of interest are viewed as random variables and the beamformer output is the maximum *a posteriori*

estimator of the signal computed in an iterative fashion. An approach based on the spatial correlation of echo signals called short-lag spatial coherence (SLSC) has been suggested in [17] and [18]. However, B-mode techniques aim at imaging the magnitude of the backscattered echoes, whereas SLSC attempts to calculate their spatial coherence. Matrone et al. [19]–[24] and Mozaffarzadeh et al. [25] presented a nonlinear beamformer called filtered-delay multiply and sum (FDMAS) that is based on computing the autocorrelation of the RF signals. This approach leads to improved resolution and contrast at the expense of high computational load, resulting in slow runtime.

Several studies investigate compressed sensing (CS) [26], [27] techniques for data reduction based on the assumption that the ultrasound signal can be sparsely represented in an appropriate basis. Wagner et al. [28] proposed a method for reducing the sampling rate by treating ultrasound signals within the finite rate of innovation [26], [27] framework. Sub-Nyquist data acquisition from each transducer element and low-rate processing were presented in [29] and were later extended to plane-wave imaging [30]. Liebgott et al. [31] studied the reconstruction performance of ultrasound signals in different bases. Liu et al. [32] introduced a beamforming technique called CS-based synthetic transmit aperture that increases the frame rate by transmitting a small number of randomly apodized plane waves and uses CS reconstruction to recover the full channel data. None of the above-mentioned works consider element reduction.

Possible approaches to reduce the number of receiving channels without compromising image quality include sub-aperture processors and microbeamformers [33], whereby part of the beamformation is moved into the probe handle. However, this requires manufacturing expensive integrated circuits with high power consumption [34]–[36]. Alternative strategies that have gained a lot of interest are based on using the standard DAS with sparse arrays where some of the elements are removed, including deterministic designs such as vernier arrays and random designs [37]–[45]. These works are concerned with designing a combined transmit/receive effective aperture mostly for 3-D imaging, whereas we propose methods that can be applied in both active and passive settings. Another approach is 2-D row–column-addressed arrays for 3-D imaging [46]–[50], in which every row and column in the array acts as one large element. However, this work is limited to 3-D imaging and the use of large elements leads to a considerable increase in edge effects that limit image quality [47].

B. Contributions

The main goal of this work it to reduce the number of receiving channels while preserving or improving the image quality in comparison with a DAS beamformer operating on the full array. To that end, we propose a new beamforming technique and present two deterministic designs of sparse arrays based on it.

We first introduce a nonlinear beamformer referred to as COnvolutional Beamforming Algorithm (COBA), which is based on the convolution of the delayed RF signals prior

to summation. COBA can be implemented efficiently using the fast Fourier transform (FFT), thus making it suitable for real-time application. We analyze the beam pattern generated by COBA and show its relation to the sum coarray [51], [52], which has twice the size of the physical aperture and triangle-shaped apodization. Consequently, COBA demonstrates significant improvement of lateral resolution and image contrast.

Then, we provide a definition of sparse arrays based on the sum coarray, which combined with COBA leads to two designs of sparse convolutional beamformers that require fewer receiving elements than DAS. The first technique, called sparse COBA (SCOBA), utilizes significantly fewer elements while obtaining a beam pattern similar to that of DAS in terms of resolution. The second method, termed SCOBA with super-resolution (SCOBAR), offers increased resolution at the expense of a smaller, yet notable, channel reduction. We then describe how to apply apodization directly on the sum coarray in order to improve its contrast. Optimization of the sparse designs reveals that the minimal number of elements required to obtain the beam patterns achieved by both SCOBA and SCOBAR is proportional to $\sqrt{N}$, where N is the number of channels in the fully populated array. Thus, these approaches offer sizable element reduction without compromising image quality.

Next, we use simulations of point reflectors and an anechoic cyst to provide qualitative and quantitative assessments of image quality using the proposed beamformers. We show that COBA achieves significant improvement of resolution and contrast compared with DAS. In addition, SCOBA and SCOBAR demonstrate a similar and enhanced performance with respect to DAS while operating with a low number of channels. These results are verified using phantom scans and in vivo cardiac data, proving that the beamformers presented are suitable for clinical use in real-time scanners.

The rest of this paper is organized as follows. In Section II, we describe the signal model and formulate our problem. Section III introduces the convolutional beamformer, applied to ultrasound image formation, and analyzes its beam pattern. We present and describe in detail sparse array designs in Section IV and propose two beamformers that utilize fewer elements. We then derive the minimal number of channels required by both approaches. In Section V, the performance of the suggested techniques is evaluated using simulated and experimental data. Finally, Section VI concludes this paper.

II. ARRAY THEORY AND PROBLEM FORMULATION

A. Signal Model and Beam Pattern

We consider a uniform linear array (ULA) comprised of $2N - 1$ transducer elements aligned along the lateral axis x. The sensor locations $\{p_n\}$ are given by

$$p_n = (nd, z = 0) \quad n = -(N-1), \ldots, N-1 \qquad (1)$$

where d is the spacing (pitch) between the centers of the individual elements and z denotes the axial axis. Upon reception, an energy pulse is backscattered from a point in space (r, θ), propagates through the tissue at speed c and is received

by all array elements at a time depending on their locations. We denote the signal received at the 0th element by

$$f(t) = \tilde{f}(t)e^{jw_0 t} \qquad (2)$$

where w_0 is the transducer center frequency and $\tilde{f}(t)$ is the signal envelope. The sensors spatially sample the signal, such that the signal $f_n(t)$ at the nth element is given by

$$f_n(t) = f(t - \tau_n) = \tilde{f}(t - \tau_n)e^{jw_0(t - \tau_n)} \qquad (3)$$

where τ_n is a time delay. To derive an expression for the delays, we introduce the following assumptions.

A 1 (Narrow Band): The signal $f(t)$ is narrow-band, i.e., the bandwidth of the envelope is small enough so that

$$\tilde{f}(t - \tau_n) \simeq \tilde{f}(t), \quad n = -(N - 1), \dots, N - 1. \qquad (4)$$

A 2 (Far Field): The point (r, θ) is in the far-field region of the array, and thus, the input signal impinging on the array is considered to be a plane wave.

Under the above-mentioned assumptions, we can rewrite (3) as

$$f_n(t) = \tilde{f}(t)e^{jw_0(t - \tau_n)} \qquad (5)$$

where $\tau_n = (d \sin \theta / c)n$, i.e., the delays are approximated by phase shifts independent of r.

A beamformer processes each sensor output by a filter with impulse response $\tilde{g}_n(t) = g_n(t + \alpha_n)$, where

$$\alpha_n = \frac{d \sin \theta_0}{c} n \qquad (6)$$

for a direction of interest $-(\pi/2) \leq \theta_0 \leq (\pi/2)$. Thus, the output of the nth element is

$$y_n(t) = \tilde{g}_n(t) \underset{t}{*} f_n(t) = g_n(t + \alpha_n) \underset{t}{*} f_n(t - \tau_n) \qquad (7)$$

where $*$ denotes temporal convolution. The beamformer then sums the outputs to obtain the array output

$$y(t) = \sum_{n=-(N-1)}^{N-1} y_n(t). \qquad (8)$$

In the frequency domain, (8) may be expressed as

$$Y(\omega) = \sum_{n=-(N-1)}^{N-1} G_n(\omega)F(\omega)e^{-j\omega(\tau_n - \alpha_n)}$$

$$= F(\omega) \sum_{n=-(N-1)}^{N-1} G_n(\omega)e^{-j\omega(\tau_n - \alpha_n)} \qquad (9)$$

where $Y(\omega)$, $F(\omega)$, and $G_n(\omega)$ are the temporal Fourier transforms of $y(t)$, $f(t)$, and $g_n(t)$, respectively.

To analyze the response of a beamformer to an input field, we assume the input to be a unity amplitude plane wave
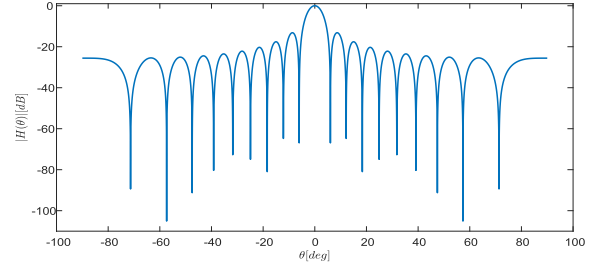
$$f(t) = e^{jw_0 t} \qquad (10)$$

Fig. 1. Beam pattern magnitude as a function of angle for $N = 10$, $w_n = 1, \lambda = 1, d = (1/2)$.

where $\tilde{f}(t) \equiv 1$. Substituting (10) into (9), we obtain

$$Y(\omega) = \delta(\omega - \omega_0) \sum_{n=-(N-1)}^{N-1} G_n(\omega)e^{-j\omega(\tau_n - \alpha_n)}$$

$$= \delta(\omega - \omega_0) \sum_{n=-(N-1)}^{N-1} G_n(\omega_0)e^{-j\omega_0(\tau_n - \alpha_n)} \qquad (11)$$

where $\delta(\omega)$ is the Dirac delta. Given the explicit expressions for τ_n and α_n, we can rewrite (11) as a function of θ

$$Y(\omega, \theta) = \delta(\omega - \omega_0) \sum_{n=-(N-1)}^{N-1} G_n(\omega_0)e^{-j\omega_0 \frac{nd}{c}(\sin\theta - \sin\theta_0)}. \qquad (12)$$

The sum on the right-hand side of (12) is defined as the beam pattern of the beamformer

$$H(\theta) \triangleq \sum_{n=-(N-1)}^{N-1} G_n(\omega_0)e^{-j\omega_0 \frac{nd}{c}(\sin\theta - \sin\theta_0)}. \qquad (13)$$

For simplicity, we assume that $\theta_0 = 0$, which yields

$$H(\theta) = \sum_{n=-(N-1)}^{N-1} G_n(\omega_0)e^{-j\omega_0 \frac{nd \sin\theta}{c}}. \qquad (14)$$

The beam pattern represents the beamformer response to variations in the input field.

In the standard DAS beamforming, we have

$$g_n(t) = w_n \delta(t), \quad n = -(N-1), \dots, N-1 \qquad (15)$$

where w_n is the weight of the nth element. Thus,

$$H_{\text{DAS}}(\theta) = \sum_{n=-(N-1)}^{N-1} w_n e^{-j\omega_0 \frac{nd \sin\theta}{c}}. \qquad (16)$$

A plot of a beam pattern generated by a standard DAS beamformer is presented in Fig. 1. The main-lobe width of the beam pattern affects system resolution, while the peak sidelobe level determines image contrast and interference levels [53].

Denote the transducer wavelength by $\lambda = 2\pi c/\omega_0$ and the array's aperture size by $L = 2(N - 1)d$. The angle θ_1 of the first zero in the beam pattern is given by

$$\sin \theta_1 = \frac{\lambda}{L}. \qquad (17)$$

Hence, a large array, or a high center frequency, yields a narrow main lobe. In contrast, the magnitude of the sidelobes is controlled by the weights $\{w_n\}$, known as the aperture function. The sidelobes can be reduced by choosing an aperture function that is smooth like a Hanning window or a Gaussian shape. This, however, broadens the main-lobe width, decreasing system resolution.

Before concluding our discussion on DAS beamforming, we note that in practice ultrasound systems perform beamforming in the digital domain: analog signals are amplified and sampled by an analog-to-digital converter [27], preceded by an antialiasing filter. Sampling rate reduction is discussed in [29]. In addition, Assumptions A1 and A2 do not typically hold in ultrasound imaging. The signal $f(t)$ is wideband and imaging is performed in the near field, leading to time delays that depend nonlinearly on both r and θ as

$$\tau_n = \frac{r + \sqrt{r^2 - 2ndr\sin\theta + (nd)^2}}{c}. \tag{18}$$

However, the approach taken here is convenient in introducing the major concepts such as in lobe and sidelobes that affect the image quality [53] and is standard in the literature.

B. Problem Formulation

The goal of this work is to design arrays with fewer elements than $2N - 1$ together with a beamforming method that enables obtaining the beam pattern given by (16) or an improved pattern in terms of resolution and image contrast. To that end, we first introduce a new beamformer based on a lateral convolution operation and show that it leads to improved resolution by analyzing its beam pattern. Next, we propose two sparse beamforming techniques. The first beamformer uses fewer channels and demonstrates a lateral resolution similar to that of DAS, whereas the second beamformer achieves a twofold improvement in resolution at the expense of a smaller element reduction. An analysis of these approaches shows that the minimal number of elements required to obtain the desired beam patterns is proportional to $\sqrt{N}$.

Throughout this paper, we assume that the element pitch d and the transducer center frequency ω_0 are fixed. In addition, we constraint the array configurations so that all element locations satisfy $|x| \le L/2$. We show that this limitation on the physical array aperture does not prevent us from creating an effective aperture that is larger in size than L. Note that we assume an odd number of elements $2N - 1$ only for clarity of presentation so that the center of the array is well-defined. However, the results presented hold also for an even number of elements.

III. Convolutional Beamforming and Its Beam Pattern

In this section, we present a new nonlinear beamformer called COBA. The proposed beamformer is based on a convolution operation and can be implemented efficiently using the FFT. We then introduce the concept of sum coarray [51], [52] to analyze the beam pattern of COBA, showing that it outperforms DAS in terms of resolution and image contrast.

A. Convolutional Beamforming

Consider the delayed signals $y_n(t)$ given by (7), where $g_n(t) = w_n\delta(t)$ as in DAS. For simplicity, we assume that unity weights $w_n = 1$. An extension for arbitrary apodization is given in Section IV-D. Inspired by the work on transmit/receive pair array synthesis [52], we define a new beamformed signal as

$$\bar{y}(t) = \sum_{n=-(N-1)}^{N-1} \sum_{m=-(N-1)}^{N-1} u_n(t)u_m(t) \tag{19}$$

where

$$u_n(t) = \exp\{j\underline{/y_n(t)}\}\sqrt{|y_n(t)|}, \quad -(N-1) \le n \le N-1 \tag{20}$$

with $\underline{/y_n(t)}$ and $|y_n(t)|$ the phase and modulus of $y_n(t)$, respectively. The operation in (20) ensures that the amplitude of each product in (19) is on the same order of that of the RF signals $y_n(t)$. This, in turn, means that the dynamic range of the resultant image will be similar to that obtained by DAS.

Computing (19) requires all possible signal pair combinations, i.e., $\binom{2N-1}{2}$ multiplications. Thus, conventionally, the computation load for each pixel is $\mathcal{O}(N^2)$, which may lead to slow runtime. This complexity can be substantially reduced by noticing that the beamformed output (19) is equivalent to

$$\bar{y}(t) = \sum_{n=-2(N-1)}^{2(N-1)} s_n(t) \tag{21}$$

where

$$s_n = \sum_{(i,j:i+j=n)} u_i(t)u_j(t), \quad n = -2(N-1), \ldots, 2(N-1). \tag{22}$$

Defining $\mathbf{s}(t)$ and $\mathbf{u}(t)$ as the length $2N - 1$ vectors whose entries are $s_n(t)$ and $u_n(t)$, receptively, we have that

$$\mathbf{s}(t) = \mathbf{u}(t) \underset{s}{*} \mathbf{u}(t) \tag{23}$$

where $\underset{s}{*}$ denotes a discrete linear convolution in the lateral direction. Thus, the vector $\mathbf{s}$ can be computed using an FFT by zero padding $\mathbf{u}$ to length $2N - 1$, compute the Fourier transform of the result, square each entry, and then perform the inverse Fourier transform to get $\mathbf{s}$. Thus, the beamformed signal $\bar{y}(t)$ is obtained with low complexity of $\mathcal{O}(N \log N)$ operations.

The temporal products comprising the signal $\bar{y}(t)$ translate to a convolution in the frequency domain with respect to the axial direction, leading to direct current and harmonic components in the spectrum of $\bar{y}(t)$ [19], [54]. Thus, an additional processing step is required to remove the baseband. The final output of our convolutional beamformer is given by

$$y_{\text{COBA}}(t) = h_{\text{BP}}(t) \underset{t}{*} \bar{y}(t) \tag{24}$$

where $h_{\text{BP}}(t)$ is a bandpass (BP) filter centered at the harmonic frequency $2\omega_0$. A summary of convolutional beamforming is presented in Algorithm 1 where the choice of weights is explained in Section IV-D.

Algorithm 1 COBA

Input: Delayed RF signals $\{y_n(t)\}$, weights $\{w_n\}$.

1: Compute $u_n(t) = \exp\{j\angle y_n(t)\}\sqrt{|y_n(t)|}$.

2: Set weights $\tilde{w}_n = \frac{w_n}{(2N-1)-|n|}$.

3: Calculate $s(t) = \mathbf{u}(t) * \mathbf{u}(t)$ using FFT.

4: Evaluate the weighted sum

$$\bar{y}(t) = \sum_{n=-2(N-1)}^{2(N-1)} \tilde{w}_n s_n(t).$$

5: Apply a band-pass filter

$$y_{\text{COBA}}(t) = h_{\text{BP}}(t) \underset{t}{*} \bar{y}(t).$$

Output: Beamformed signal $y_{\text{COBA}}(t)$.

We note that COBA involves computing pairwise products of the RF signals as in FDMAS. However, in contrast to FDMAS, it consists of all possible products, including the self-products for $n = m$ and repetitions created by interchanging n and m. This allows to avoid the high computational complexity and partial energy loss which FDMAS suffers from [55]. In addition, the works related to FDMAS did not consider element reduction that is the main contribution of this paper and is described in Section IV.

B. Beam Pattern Analysis

We now analyze the beam pattern of the proposed convolutional beamformer to show that it outperforms the standard DAS beamforming in terms of lateral resolution and image contrast. To this end, we use the following definitions.

Definition 1 (Position Set): Consider a linear array with d the minimum spacing of the underlying grid on which sensors are assumed to be located. The *position set* is defined as an integer set I, where $n \in I$ if there is a sensor located at nd.

In the interest of brevity, we refer to a linear array with position set I as a linear array I.

Definition 2 (Sum Coarray): Consider a linear array I. Define the set

$$\widetilde{S}_I = \{n + m : n, m \in I\}. \tag{25}$$

Note that $\widetilde{S}_I$ includes repetitions of its elements. We also define the set S_I, referred to as the sumset of I, which consists of the distinct elements of $\widetilde{S}_I$. The *sum coarray* of I is defined as the array whose position set is S_I.

As an example, the sum coarray of an M element ULA is another ULA with $2M - 1$ elements. The number of elements in the sum coarray directly determines the number of nonzeros in the convolutional signal given by (23).

Definition 3 (Intrinsic Apodization): Consider a linear array I and define a binary vector $\mathbb{1}_I$ whose nth entry is 1 if $n \in I$ and zero otherwise. The *intrinsic apodization* is an integer vector defined as

$$\mathbf{a} = \mathbb{1}_I * \mathbb{1}_I. \tag{26}$$

The intrinsic apodization vector is related to S_I and $\widetilde{S}_I$ in the following way. For every $n \in S_I$, the entry a_n denotes the number of occurrences of n in $\widetilde{S}_I$.

To derive an expression for the beam pattern of the convolutional beamformer, we assume the input signal to be $f(t) = e^{j\omega_0 t}$ impinging on the array at direction θ, as in Section II. Consequently, we obtain

$$u_n(t) = e^{j\omega_0 t} e^{-j\omega_0 \tau_n} \tag{27}$$

where τ_n is given by (5). Substituting (27) into (19), we have

$$\bar{y}(t) = \sum_{n=-(N-1)}^{N-1} \sum_{m=-(N-1)}^{N-1} e^{j2\omega_0 t} e^{-j\omega_0(\tau_n + \tau_m)}$$

$$= e^{j2\omega_0 t} \sum_{n,m=-(N-1)}^{N-1} e^{-j\omega_0(\tau_n + \tau_m)}. \tag{28}$$

Following BP filtering, we get

$$y_{\text{COBA}}(t) = \left(h_{\text{BP}}(t) \underset{t}{*} e^{j2\omega_0 t}\right) \sum_{n,m=-(N-1)}^{N-1} e^{-j\omega_0(\tau_n + \tau_m)}. \tag{29}$$

In the Fourier domain

$$Y_{\text{COBA}}(\omega) = \delta(\omega - 2\omega_0) H_{\text{BP}}(2\omega_0) \sum_{n,m=-(N-1)}^{(N-1)} e^{-j\omega_0(\tau_n + \tau_m)} \tag{30}$$

where $H_{\text{BP}}(\omega)$ is the Fourier transform of the BPF $h_{\text{BP}}(t)$. Assuming that $H_{\text{BP}}(2\omega_0) = 1$, the beam pattern generated by COBA is

$$H_{\text{COBA}}(\theta) = \sum_{n,m=-(N-1)}^{N-1} e^{-j\omega_0(\tau_n + \tau_m)}$$

$$= \sum_{n,m=-(N-1)}^{N-1} e^{-j\omega_0 \frac{d\sin\theta}{c}(n+m)} \tag{31}$$

where the last equation is obtained by substituting the explicit expression for τ_n.

The sum in (31) is the product of two polynomials $H_{\text{COBA}}(\theta) = H_{\text{DAS}}(\theta) H_{\text{DAS}}(\theta)$ with $H_{\text{DAS}}(\theta)$ given by (16) assuming $w_n = 1$. In Appendix A, we show that $H_{\text{COBA}}(\theta)$ can be written as a single polynomial

$$H_{\text{COBA}}(\theta) = \sum_{n=-2(N-1)}^{2(N-1)} a_n e^{-j\omega_0 \frac{d\sin\theta}{c}n} \tag{32}$$

where $\{a_n\}$ are triangle-shaped intrinsic apodization weights given by (26). This apodization is illustrated in Fig. 5(b) and is further discussed in Section IV-D.

Equation (32) can be thought of as the beam pattern of a DAS beamformer operating on the sum coarray. This virtual array is twice the size of the physical one, leading to a resolution, that is twice better the standard resolution. In addition, the apodization of the sum coarray reduces the sidelobes, and thus, the convolutional beamformer results in improved image contrast, as demonstrated in Fig. 2.
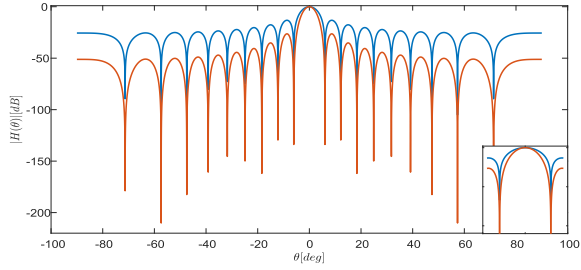
Fig. 2. Beam pattern magnitude of DAS (blue line) and COBA (red line) for $N = 10$, $w_n = 1$, $\lambda = 1$, and $d = (1/2)$. Bottom-right corner: zoomed-in view on the main lobes.

IV. SPARSE CONVOLUTIONAL BEAMFORMING

So far, we presented a convolutional beamformer that leads to better resolution and contrast with respect to DAS. An analysis of its beam pattern showed that its performance depends on the sum coarray rather than the physical array. In this section, we exploit this property to derive two families of beamformers that rely on a reduced number of elements, without affecting the beam pattern.

A. Sparse Arrays

Given a ULA of $2N - 1$ elements with position set $I = \{-(N-1), \ldots, (N-1)\}$, we aim to remove some of its elements to create a thinned array. The challenge is to design such an array without degrading image quality. To this end, we define the following.

Definition 4 (Sparse Array): Consider a ULA with position set I. A *sparse array* with respect to I is a thinned array, created by removing part of the elements, which satisfies

$$J \subset I \subseteq S_J \tag{33}$$

where J and S_J are integer sets indicating the elements positions of the thinned array and of its sum coarray, respectively.

A sparse array J according to Definition 4 must be a strict subarray of I, i.e., the number of elements in J is strictly smaller than that of I. In addition, performing convolutional beamforming using J is equivalent to applying DAS beamforming on the sum coarray S_J which by Definition 4 has an aperture at least as large as the original ULA I. Thus, it results in a beam pattern that is equal or better in resolution than the beam pattern generated by a DAS beamformer applied to I.

B. Sparse Beamforming

Here, we provide a simple closed-form sparse array design that leads to a large element reduction.

Assume that N is not prime, so that it can be factored as $N = AB$, where $A, B \in \mathbb{N}^+$. Given such a decomposition, we define the following array:

$$U_A = \{-(A-1), \ldots, 0, \ldots, A-1\},$$
$$U_B = \{nA : n = -(B-1), \ldots, 0, \ldots, B-1\}. \tag{34}$$

An illustration of this array for $N = 9$, $A = 3$, and $B = 3$ is seen in Fig. 3.

Let $U_A + U_B = \{n + m : n \in U_A, m \in U_B\}$. Then,

$$U_A + U_B = \{-(AB - 1), \ldots, 0, \ldots, AB - 1\}$$
$$= \{-(N-1), \ldots, 0, \ldots, N-1\}$$
$$= I. \tag{35}$$

Thus, denoting by $U \subset I$ the array geometry defined as

$$U = U_A \cup U_B \tag{36}$$

it holds that

$$I \subset S_U \tag{37}$$

where S_U is the sumset of U. Thus, the family of sets (36) satisfies (33), where the number of elements in each set is $2A + 2B - 3$. As an example, for $N = 9$, $A = 3$, and $B = 3$, the set U has only 9 elements out of 17 in the full array, as shown in Fig. 3. We note that the proposed sparse arrays are similar to nested arrays [56] used in the array processing literature. However, while nested arrays are related to the difference coarray, the sets (34) are synthesized from the sum coarray perspective [51] and have a smaller physical aperture.

Based on U, we propose SCOBA that computes the following signal:

$$\bar{y}_{\text{SCOBA}}(t) = \sum_{n \in U} \sum_{m \in U} u_n(t) u_m(t) \tag{38}$$

where $u_n(t)$ is defined in (20). Namely, we perform COBA only on the outputs of the elements in U. As before, (38) can be written using the sum coarray S_U

$$\bar{y}_{\text{SCOBA}}(t) = \sum_{n \in S_U} s_n(t) \tag{39}$$

where

$$s_n(t) = \sum_{(i,j \in U : i+j=n)} u_i(t) u_j(t). \tag{40}$$

The final output of SCOBA is given by

$$y_{\text{SCOBA}}(t) = h_{\text{BP}}(t) * \bar{y}_{\text{SCOBA}}(t). \tag{41}$$

Computing (39) can be performed using appropriate zero padding and FFT in $\mathcal{O}(N \log N)$ operations or directly by pairwise products with complexity $\mathcal{O}((A+B)^2)$ that may be lower. The proposed beamformer is summarized in Algorithm 2.

To analyze the beam pattern produced by SCOBA, we follow the same steps presented in Section III. This leads to

$$H_{\text{SCOBA}}(\theta) = \sum_{n,m \in U} e^{-j\omega_0 \frac{d \sin\theta}{c}(n+m)}$$
$$= \sum_{n \in S_U} u_n e^{-j\omega_0 \frac{d \sin\theta}{c} n} \tag{42}$$

where $\mathbf{u} = \mathbb{1}_U * \mathbb{1}_U$ is the intrinsic apodization of SCOBA. Notice that (42) can be rewritten as

$$H_{\text{SCOBA}}(\theta) = \sum_{n \in I} u_n e^{-j\omega_0 \frac{d \sin\theta}{c} n} + \sum_{m \in S_U/I} u_m e^{-j\omega_0 \frac{d \sin\theta}{c} m} \tag{43}$$

where $S_U/I = \{m \in S_U : m \notin I\}$. The first sum in (43) ensures that the resolution of SCOBA is at least as good as the
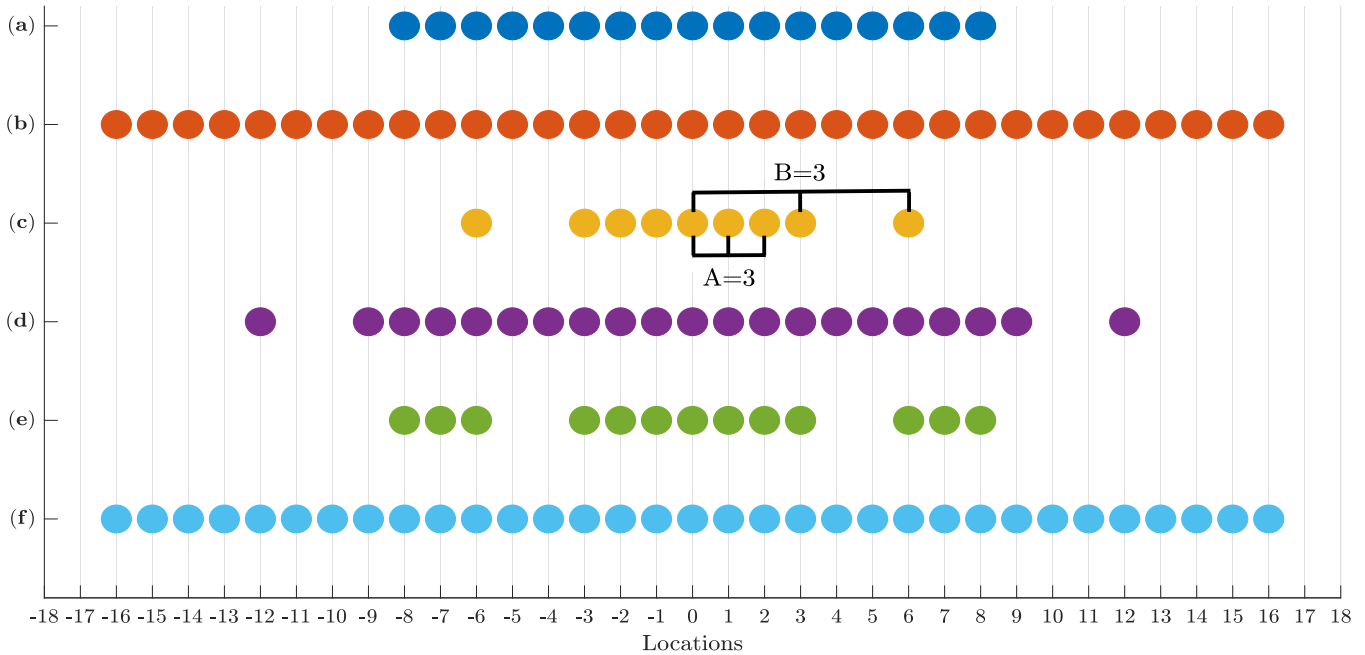
Fig. 3. Element positions of (a) ULA $I = [-8, 8]$, (b) sum coarray $S_I = [-16, 16]$, (c) sparse array U given by (36), (d) sum coarray S_U, (e) sparse array V defined by (45), and (f) sum coarray S_V. In this example, the element spacing is $d = 1$, $N = 9$, $A = 3$, and $B = 3$.

Algorithm 2 SCOBA

Input: Delayed RF signals $\{y_n\}$, weights $\{w_n\}$, parameters A, B.

1: Construct the set U using (36) and its sumset S_U.

2: Compute $u_n(t) = \exp\{j \angle y_n(t)\}\sqrt{|y_n(t)|}$, $n \in U$.

3: Calculate $\mathbf{a} = \mathbb{1}_U * \mathbb{1}_U$.

4: Set weights $\tilde{w}_n = \frac{w_n}{a_n}$, $n \in S_U$.

5: For all $n \in S_U$ compute $s_n(t)$ using (40).

6: Evaluate the weighted sum

$$\bar{y}(t) = \sum_{n \in S_U} \tilde{w}_n s_n(t).$$

7: Apply a band-pass filter

$$y_{\text{SCOBA}}(t) = h_{\text{BP}}(t) \underset{t}{*} \bar{y}(t).$$

Output: Beamformed signal $y_{\text{SCOBA}}(t)$.

Fig. 4. Beam pattern of DAS (blue line), SCOBA (red line), and SCOBAR (yellow line) for $N = 6$ $A = 3$, $B = 2$, $\lambda = 1$, and $d = (1/2)$.

coupling [57]–[60], which is the electromagnetic interaction between adjacent sensors that has an adverse effect on obtaining a desired beam pattern. In Section IV-E, we discuss how to minimize the number of sensors using this approach.

resolution of a DAS beamformer applied on the full array I. The second sum, on the right-hand side of (43), provides additional degrees of freedom that may be used to improve the resolution. The image contrast depends on the apodization $\{u_n\}$, which can be adjusted as we describe in Section IV-D. A demonstration of the beam pattern of SCOBA is presented in Fig. 4.

The number of elements required for SCOBA is $2A + 2B - 3$, and thus, it leads to a family of beamformers in which each beamformer demonstrates a different level of element reduction, controlled by the parameters A and B. While a large number of elements may be favorable in the presence of noise, it also increases the mutual
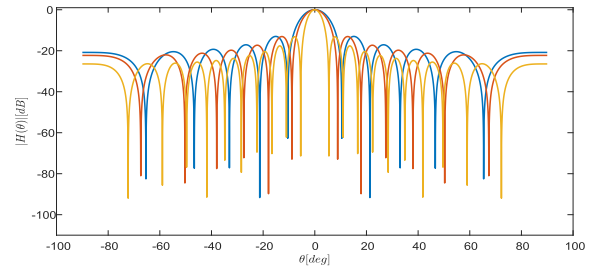
C. Sparse Beamforming With Super-Resolution

Previously, we presented COBA that achieves double the standard resolution. Following that, we introduced a sparse array design to create a beamformer, which uses fewer elements and yields a resolution that is comparable with the standard one. Now, we propose a family of sparse beamformers with enhanced resolution that is equivalent to that of COBA, thereby combining the best of both worlds. We refer to this technique as SCOBAR.

We extend the array configuration used in SCOBA by constructing an additional array as
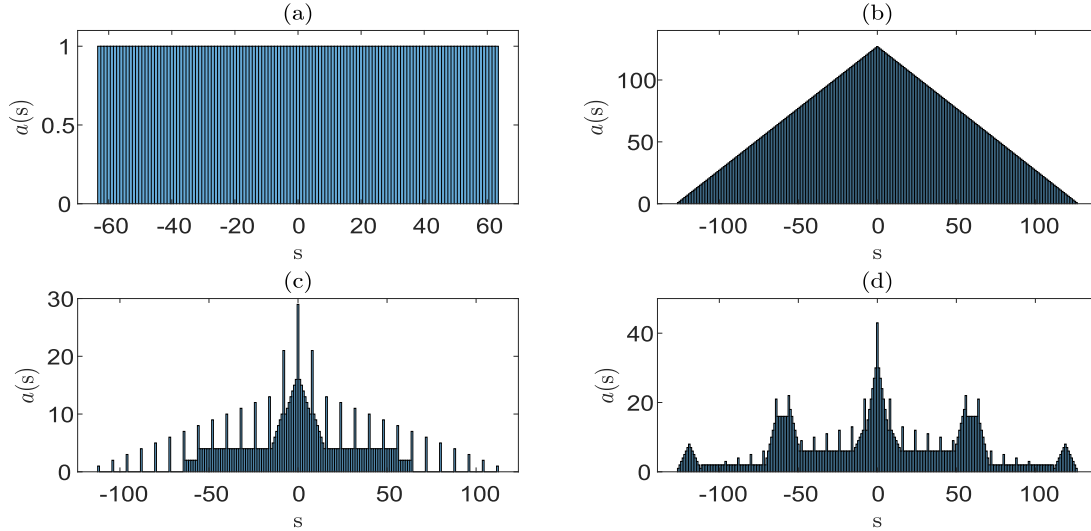
$$U_C = \{n : |n| = N - A, \dots, N - 1\}. \tag{44}$$

Fig. 5. Intrinsic apodization of (a) DAS with 127 elements, (b) COBA with 127 elements, (c) SCOBA with $A = B = 8$, and (d) SCOBAR with $A = B = 8$.

Then, we define a sparse array geometry given by

$$V = U_A \cup U_B \cup U_C. \tag{45}$$

As shown in Fig. 3, we obtain V by adding to U two small ULAs of size $A - 1$ at its edges. It can be verified that

$$V \subset I \subset S_V = S_I \tag{46}$$

i.e., the sum coarray of V is equal to the sum coarray of the full array I. SCOBAR uses the array sensors given by V to compute the signal

$$\bar{y}_{\text{SCOBAR}}(t) = \sum_{n \in V} \sum_{m \in V} u_n(t) u_m(t)$$
$$= \sum_{n \in S_V} s_n(t) \tag{47}$$

where $u_n(t)$ is defined in (20) and

$$s_n(t) = \sum_{(i,j \in V : i+j=n)} u_i(t) u_j(t). \tag{48}$$

The final output of SCOBAR is given by

$$y_{\text{SCOBAR}}(t) = h_{\text{BP}}(t) * \bar{y}_{\text{SCOBAR}}(t). \tag{49}$$

Similar to SCOBA, (47) can be calculated using the FFT in $\mathcal{O}(N \log N)$ operations or directly in $\mathcal{O}((A + B)^2)$. A summary of SOCBAR is provided in Algorithm 3.

Following similar arguments as for COBA and SCOBA, the beam pattern of SCOBAR is:

$$H_{\text{SCOBAR}}(\theta) = \sum_{n,m \in V} e^{-j\omega_0 \frac{d \sin\theta}{c}(n+m)}$$
$$= \sum_{n \in S_V} v_n e^{-j\omega_0 \frac{d \sin\theta}{c} n}$$
$$= \sum_{n=-2(N-1)}^{2(N-1)} v_n e^{-j\omega_0 \frac{d \sin\theta}{c} n} \tag{50}$$

where $\mathbf{v} = \mathbb{1}_V * \mathbb{1}_V$ and the last equality is due the fact that $S_V = S_I = \{-2(N-1), \ldots, 2(N-1)\}$. The latter implies that the lateral resolution of SCOBAR is similar to that of COBA,
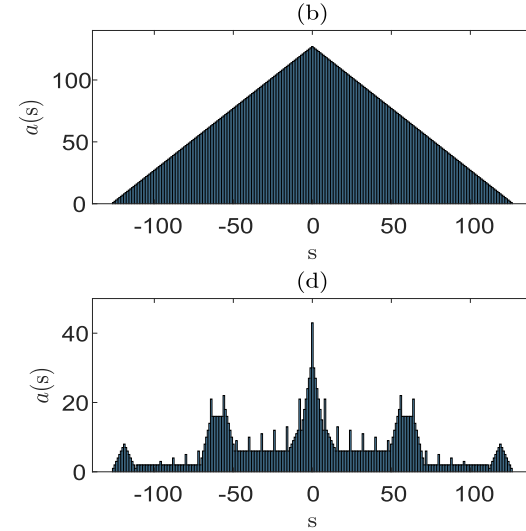
Algorithm 3 SCOBAR

Input: Delayed RF signals $\{y_n\}$, weights $\{w_n\}$, parameters A, B.

1: Construct the set V using (45) and its sumset S_V.
2: Compute $u_n(t) = \exp\{j\underline{/y_n(t)}\}\sqrt{|y_n(t)|}$, $n \in V$.
3: Calculate $\mathbf{a} = \mathbb{1}_V * \mathbb{1}_V$.
4: Set weights $\tilde{w}_n = \frac{w_n}{a_n}$, $n \in S_V$.
5: For all $n \in S_V$ compute $s_n(t)$ using (48).
6: Evaluate the weighted sum

$$\bar{y}_{\text{SCOBAR}}(t) = \sum_{n \in S_V} \tilde{w}_n s_n(t).$$

7: Apply band-pass filter

$$y_{\text{SCOBAR}}(t) = h_{\text{BP}}(t) * \bar{y}_{\text{SCOBAR}}(t).$$

Output: Beamformed signal $y_{\text{SCOBAR}}(t)$.

twofold better than the standard one, as shown in Fig. 4. The weights $\{v_n\}$ can be modified to control the image contrast as described in Section IV-D.

The number of elements required by SCOBAR is $4A + 2B - 5$, and thus, the improved resolution is at the expense of a smaller element reduction in comparison with SCOBA. Optimization of the parameters A and B is presented in Section IV-E.

D. Apodization

As stated in Section II, the image contrast is governed by the peak sidelobe level. Amplitude apodization [61] is an important tool used for suppressing sidelobes, leading to improved contrast. Typical apodization functions include Hanning, Hamming, or Gaussian amplitude weighting of the elements that lowers the sidelobes at the expense of widening the main lobe width, i.e., worsening the lateral resolution. Therefore, there is a tradeoff between lateral resolution and contrast and a judicious choice of the apodization must be made based on the clinical application.

In Section III-B, we introduced the concept of intrinsic apodization that arises in the proposed beamformers. This concept is extended to a standard DAS beamformer by assuming that the array has intrinsic weights of unity. Fig. 5 shows the intrinsic apodization of the different beamformers. For a DAS beamformer, the intrinsic apodization function is constant over the elements and equal to 1, whereas for COBA, we get a triangle-shaped apodization that suppresses sidelobes. The intrinsic apodization functions of SCOBA and SCOBAR depend on the parameters A and B and should be analyzed to avoid unwanted sidelobes.

To address this issue, we propose a simple adjustment to the apodization function that takes into account the intrinsic apodization. Given a desired apodization function with weights $\{w_n\}$, we define a modified apodization function

$$\tilde{w}_n = \frac{w_n}{a_n} \tag{51}$$

where $\{a_n\}$ are the intrinsic weights assumed to be nonzero. Then, we apply these weights on the sum coarray by computing the weighted sum

$$\bar{y}(t) = \sum_n \tilde{w}_n s_n(t) \tag{52}$$

prior to BP filtering. This ensures that the resulting beam pattern will have weights equal to $\{w_n\}$ as desired.

The intrinsic apodization functions of both COBA and SCOBAR have only nonzeros, and thus, any apodization can be achieved using (51). In the case of SCOBA, the intrinsic apodization has zeros, leading to discontinuities in the beam pattern which may be considered as a drawback at first glance. However, note that this is expected since the intrinsic apodization of SCOBA is designed to have nonzeros in the range $-[N-1, N-1]$, similar to the DAS beamformer. Thus, any apodization function obtained by DAS can be attained by SCOBA. In fact, the intrinsic apodization of SCOBA has more degrees of freedom (nonzeros) than DAS as shown in (43), allowing the use of an extended family of apodization functions.

E. Minimal Number of Elements

As noted before, the number of elements used by SCOBA and SCOBAR is controlled by the parameters A and B. We next derive the expressions for A and B, leading to a minimal number of sensors required by the proposed beamformers.

For SCOBA, minimizing the number of elements can be cast as the following optimization problem:

$$A^*, B^* = \underset{A, B \in \mathbb{N}}{\arg\min}\ 2(A + B) - 3$$
$$\text{s.t. } AB = N. \tag{53}$$

When N is a prime number, there are only two feasible solutions that are optimal given by $A = N$ and $B = 1$ and vice versa; both result in a fully populated array. Hence, we consider below the case where N is not prime and (53) becomes a combinatorial optimization problem. A closed-form solution is presented in Theorem 1.
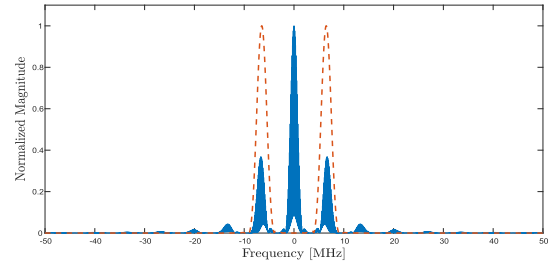

Fig. 6. Fourier transforms of the impulse response of the Hanning-based BP filter (dashed line) and of the signal given by (21), which corresponds to the central simulated image line.

Theorem 1: Given an arbitrary $N \in \mathbb{N}^+$, define the sets

$$D_1 = \{m \in \mathbb{N} : m|N,\ m \le \sqrt{N}\}$$
$$D_2 = \{m \in \mathbb{N} : m|N,\ m \ge \sqrt{N}\} \tag{54}$$

where $m|N$ indicates that m is a divisor of N. The optimal solutions for (53) are

$$A^* = \max(D_1) \quad \text{and} \quad B^* = \min(D_2)$$
$$A^* = \min(D_2) \quad \text{and} \quad B^* = \max(D_1). \tag{55}$$

When N is a perfect square, we have a single optimal solution

$$A^* = B^* = \sqrt{N}. \tag{56}$$

Proof: Here, we prove the case where N is a perfect square. The complete proof is given in Appendix B.

First, we write an equivalent problem to (53) as

$$A^*, B^* = \underset{A, B \in \mathbb{N}}{\arg\min}\ A + B$$
$$\text{s.t. } AB = N. \tag{57}$$

From the inequality of the arithmetic and geometric means, we have that

$$\sqrt{AB} \le \frac{A + B}{2}. \tag{58}$$

Thus, the objective function is lower bounded by $2\sqrt{N}$. Equality is obtained in (58) if and only if $A = B = \sqrt{N}$. Thus, this choice attains the lower bound and is optimal, which concludes the proof. ∎

Theorem 1 implies that the minimal number of elements required by SCOBA is proportional to $\sqrt{N}$ and the beamformed signal given by (49) can be computed with a low complexity of $\mathcal{O}(N)$.

As for SCOBAR, note that when $B = 1$, $U_C = U_A$, and $A = N$, leading to the trivial case where the array is full, hence, we assume that $B > 1$. In this case, the minimal number of elements required by SCOBAR is given by the solution to

$$A^*, B^* = \underset{A, B \in \mathbb{N},\ B > 1}{\arg\min}\ 2(2A + B) - 5$$
$$\text{s.t. } AB = N. \tag{59}$$

When N is prime, the only feasible and, hence, optimal solution is $A = 1$ and $B = N$, which is trivial. Therefore, we address below the case where N is not prime. A closed-form solution is obtained in Theorem 2.
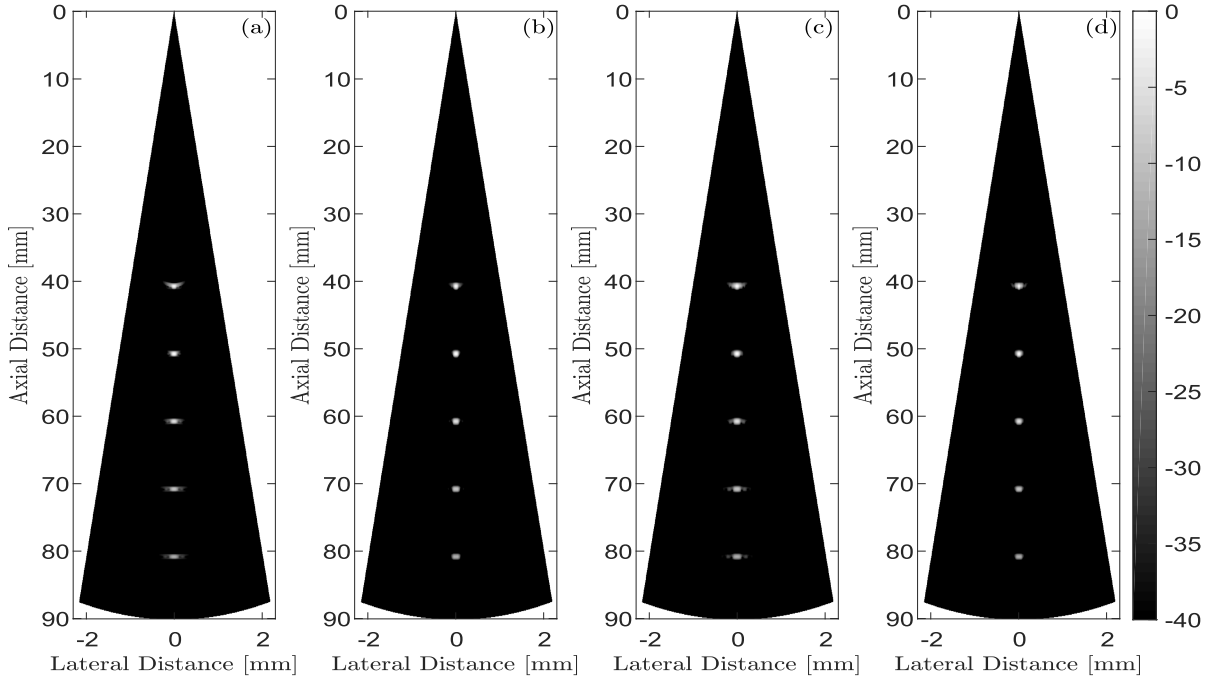
Fig. 7. Images of simulated point-reflector phantom obtained by (a) DAS (127), (b) COBA (127), (c) SCOBA (29), and (d) SCOBAR (43). Number in brackets refers to the number of elements used.

Theorem 2: Given an arbitrary $N \in \mathbb{N}^+$, define the sets

$$D_3 = \{m \in \mathbb{N} : m|2N, m \leq \sqrt{2N}\}$$
$$D_4 = \{m \in \mathbb{N} : m|2N, m \geq \sqrt{2N}\}. \quad (60)$$

Denote by $\mathbb{E}$ the set of even integers. The optimal solutions for (59) are given by the following cases.

1) $\max(D_3) \in \mathbb{E}$, $\min(D_4) \in \mathbb{E}$

$$A^* = \max(D_3)/2 \quad \text{and} \quad B^* = \min(D_4)$$
$$A^* = \min(D_4)/2 \quad \text{and} \quad B^* = \max(D_3). \quad (61)$$

2) $\max(D_3) \in \mathbb{E}$, $\min(D_4) \notin \mathbb{E}$

$$A^* = \max(D_3)/2 \quad \text{and} \quad B^* = \min(D_4). \quad (62)$$

3) $\max(D_3) \notin \mathbb{E}$, $\min(D_4) \in \mathbb{E}$

$$A^* = \min(D_4)/2 \quad \text{and} \quad B^* = \max(D_3). \quad (63)$$

When $2N$ is a perfect square, there is a single solution

$$A^* = \frac{\sqrt{2N}}{2}, \quad B^* = \sqrt{2N}. \quad (64)$$

Proof: Here, we provide the proof only for the special case when $2N$ is a perfect square. The proof for the general case is detailed in Appendix C.

Problem (59) is equivalent to

$$A^*, B^* = \underset{A,B \in \mathbb{N}, B>1}{\arg\min} \quad 2A + B$$
$$\text{s.t. } AB = N. \quad (65)$$

Once more, using the inequality of arithmetic and geometric means, we get

$$\sqrt{2AB} \leq \frac{2A + B}{2}. \quad (66)$$

Consequently, the objective value is lower bounded by $2\sqrt{2N}$. This bound is attained by choosing $A = \sqrt{(N/2)}$ and $B = \sqrt{2N}$. $\qquad\square$

Theorem 2 indicates that SCOBAR requires a minimal number of sensors that are on the order of $\sqrt{2N}$. The beamformed signal can be obtained in complexity $\mathcal{O}(N)$ similar to SCOBA. Note, however, that while SCOBAR demonstrates almost twofold improvement in resolution, the increase in the number of elements, compared with SCOBA, is roughly only by a factor of $\sqrt{2}$.

F. Minimal Physical Aperture

With the purpose of reducing cost and size, one may desire to design a compact probe with a small physical aperture. While the size of the physical aperture using COBA and SCOBAR is fixed and given by $L = (2N - 1)d$, for SCOBA, it is equal to $\tilde{L} = 2A(B - 1)d$, where $B > 1$, and thus can be minimized using an appropriate choice of A and B. This objective can be formulated as follows:

$$A^*, B^* = \underset{A,B \in \mathbb{N}, B>1}{\arg\min} \quad A(B - 1)$$
$$\text{s.t. } AB = N. \quad (67)$$

The solution to (67) is given by Theorem 3.

Theorem 3: Consider a nonprime number $N \in \mathbb{N}^+$. Denote by D the set of the nontrivial divisors of N, defined as

$$D = \{m \in \mathbb{N} : m|N, 1 < m < N\}. \quad (68)$$
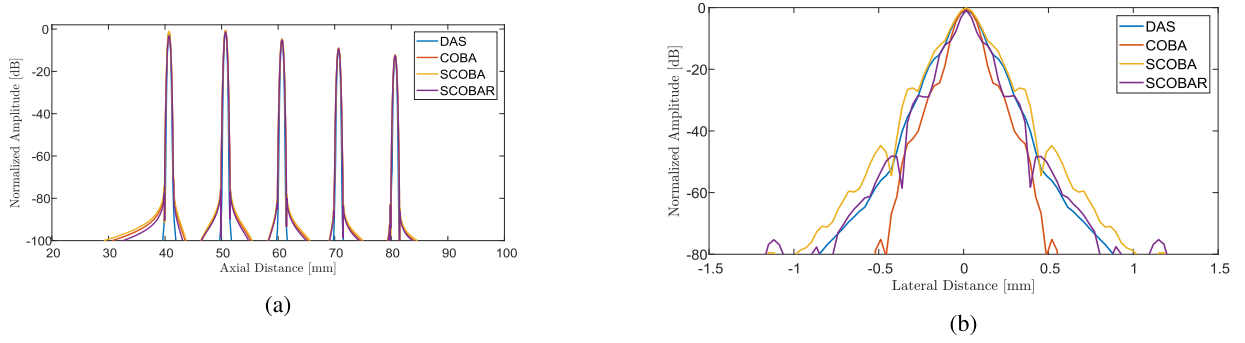
Fig. 8.   (a) Axial profiles of all four methods at the center image line. (b) Lateral cross sections of all four techniques at a focal depth of 50 mm.
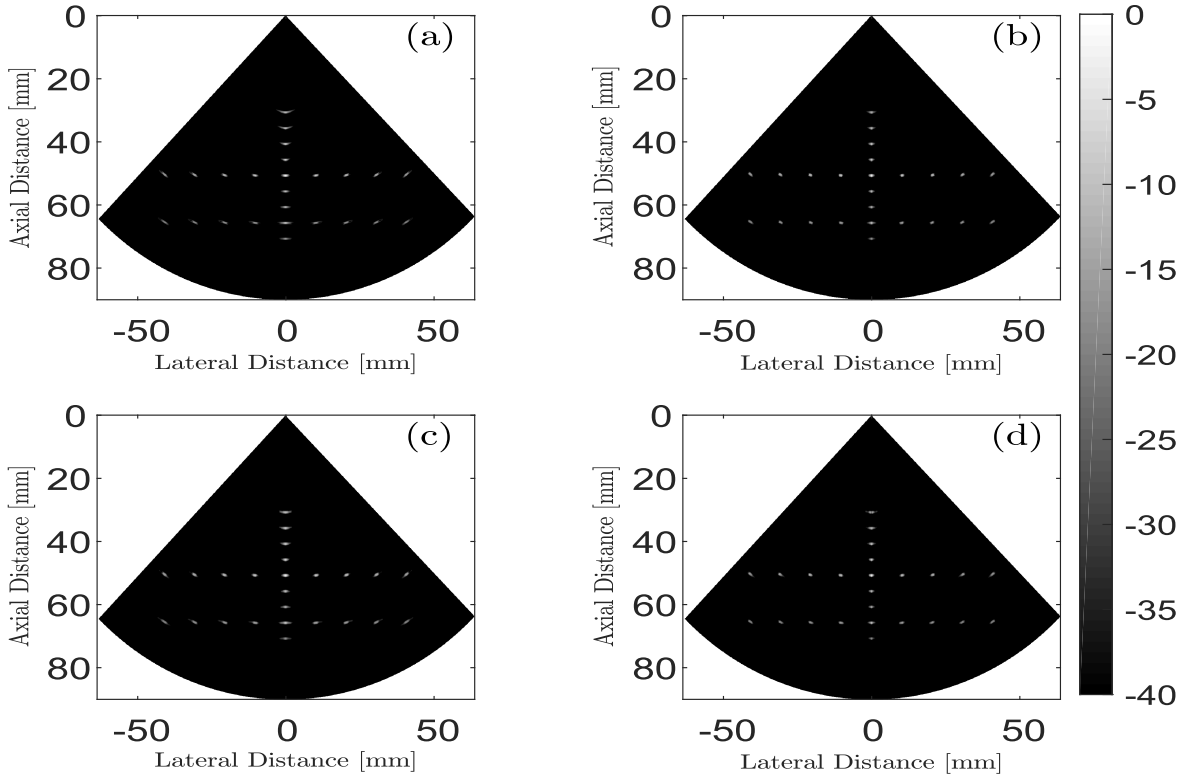

Fig. 9.   Images of simulated on-axis and off-axis point targets obtained by (a) DAS (127), (b) COBA (127), (c) SCOBA (29), and (d) SCOBAR (43). Number in brackets refers to the number of elements used.

Then, the optimal solution to (67) is

$$A^* = \max(D), \quad B^* = \min(D). \tag{69}$$

Proof: Using the fact that $A(B - 1) = N - A$, we rewrite (67) as

$$A^*, B^* = \underset{A,B \in \mathbb{N}, \, B > 1}{\arg\max} \quad A$$
$$\text{s.t. } AB = N. \tag{70}$$

It is easy to see from (70) that the optimal A is the maximal nontrivial divisor of N, i.e., $A^* = \max(D)$. Consequently, $B^* = (N/A^*) = \min(D)$, which concludes the proof.   □

Theorem 3 implies that when $N = 2M$ with $M \in \mathbb{N}^+$, the optimal choice is $A = M$ and $B = 2$, which leads to a ULA with a physical aperture that is twice of that of the original ULA. In other words, performing SCOBA on a given ULA is equivalent to performing COBA on a ULA with half the size. Note, however, that the number of elements in this case is $2M+1 = N+1$, which is much larger than the minimal number achieved by Theorem 1.

V. EVALUATION RESULTS

We now verify the performance of the proposed beamformers in comparison with DAS. The resolution and contrast are first evaluated using Field II simulator [62], [63] in MATLAB. Following that, we apply the methods on phantom data, scanned using a Verasonics imaging system, and on *in vivo* cardiac data acquired from a healthy volunteer.

In the following experiments, we do not apply apodization upon reception for DAS and COBA. For a fair comparison, we employ weights in SCOBA to create an effective apodization of ones as in DAS. For SCOBAR, we apply weights to yield an effective triangle-shaped apodization as in COBA.
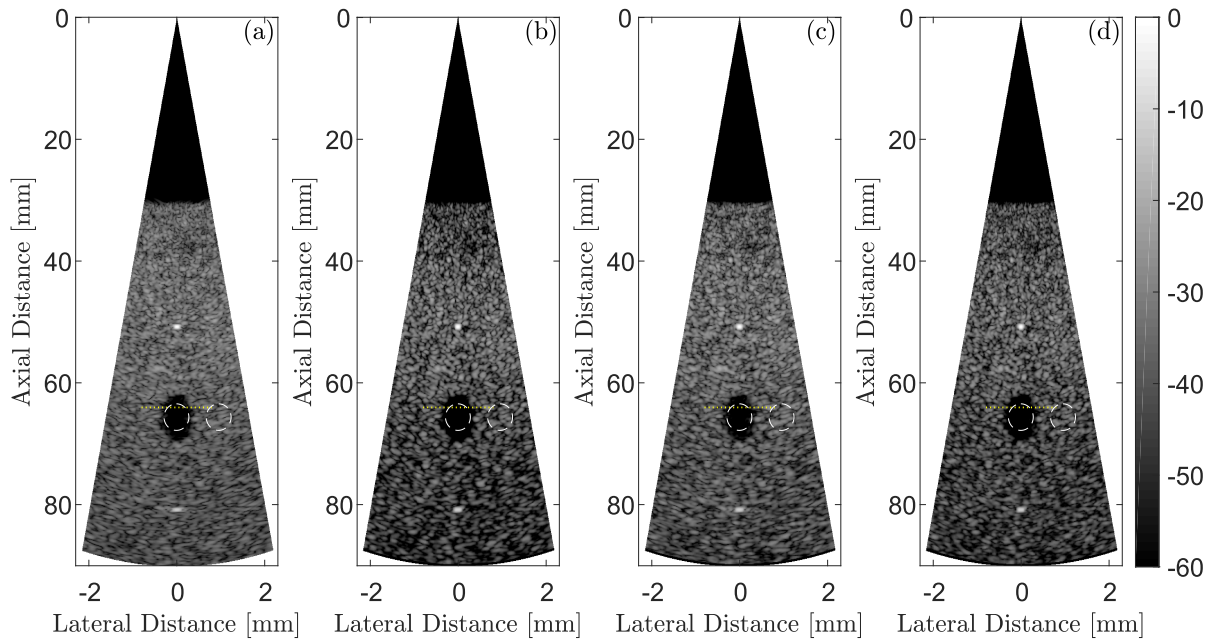
Fig. 10. Images of simulated anechoic cyst phantom obtained by (a) DAS (127), (b) COBA (127), (c) SCOBA (29), and (d) SCOBAR (43). The dashed line marks the lateral cross section presented in Fig. 11. The dashed circles indicate the region used for computing the CRs. Number in brackets refers to the number of elements used.

The full transducer array is used for transmission, and element reduction is performed only on the receiving end.

A. Simulations

In both simulations presented here, we used an array consisting of 127 elements with an element width of 440 μm, a height of 6 mm, and a kerf of 0.0025 mm. During transmission, the transducer generated a Hanning-windowed 2-cycle sinusoidal pulse with a center frequency of 3.5 MHz and a focal depth of 50 mm.

In COBA, SCOBA, and SCOBAR, a BP filter was applied using a Hanning window. The window frequency boundaries were empirically determined to well isolate the signal band to be preserved (see Fig. 6). The sampling frequency was 100 MHz. For SCOBA and SCOBAR, we used $A = B = 8$, which leads to the minimal numbers of 29 (23%) and 43 (34%) elements, respectively, according to Theorems 1 and 2.

1) Resolution: We evaluate resolution using a point-reflector simulated phantom with isolated scatterers distributed in an anechoic background. Fig. 7 presents the results of DAS, COBA, SCOBA, and SCOBA. As seen from the images, SCOBA has achieved a comparable lateral resolution to that of DAS while using fewer elements. COBA outperforms DAS in terms of lateral resolution, which is seen clearly in the focal depth and beyond it. SCOBAR obtains similar results to COBA using fewer elements. For a closer look, the center image line and the lateral cross section of the scattering point placed at the transmission focus in 50 mm are shown in Fig. 8. One can observe from Fig. 8(a) that all four methods have a similar axial resolution. In terms of lateral resolution, the performance of SCOBA is the same as DAS, while SCOBAR is better than DAS and COBA outperforms them all. Fig. 9 shows the similar results obtained through
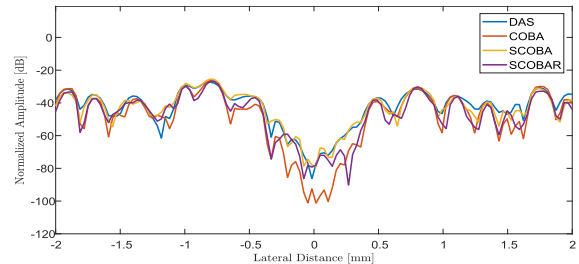

Fig. 11. Lateral cross sections of the cyst obtained by all four techniques.

a simulation that includes on-axis targets as well as off-axis targets.

2) Contrast: For contrast evaluation, we use a simulated phantom of an anechoic cyst embedded in a speckle background. Fig. 10 displays the images obtained with DAS, COBA, SCOBA, and SCOBAR and provides a qualitative impression of the contrast achieved by each method. In addition, lateral cross sections of the cyst at a depth of 64 mm (dashed line in Fig. 10) are presented in Fig. 11, showing that SCOBA and DAS have a similar contrast, SCOBAR demonstrates an improvement over the latter, and COBA achieves the best performance.

A quantitative measure of contrast is the contrast ratio (CR) [17]

$$CR = 20 \log_{10}\left(\frac{\mu_{\text{cyst}}}{\mu_{\text{bck}}}\right) \tag{71}$$

where μ_{cyst} and μ_{bck} are the mean image intensities, prior to log-compression, computed over small regions inside the cyst and in the surrounding background, respectively. The regions selected are designated by the dashed circles in Fig. 10. Consistent with the previous results, the CR of DAS is
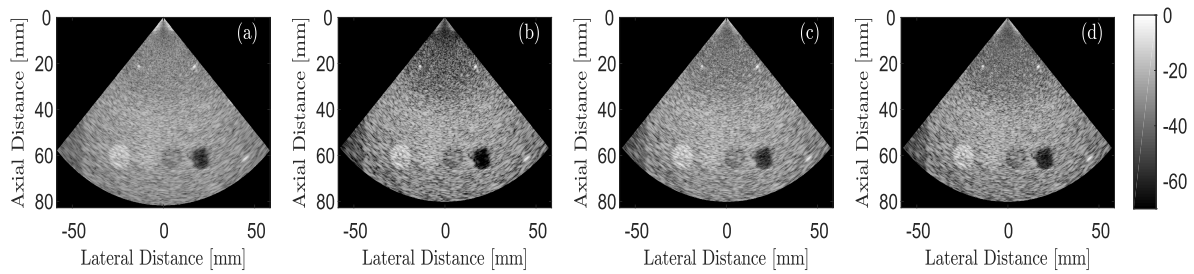
Fig. 12. Images of GAMMEX 403GSLE which include pin and cystic targets obtained with (a) DAS (63), (b) COBA (63), (c) SCOBA (21), and (d) SCOBAR (29). Number in brackets refers to the number of elements used.
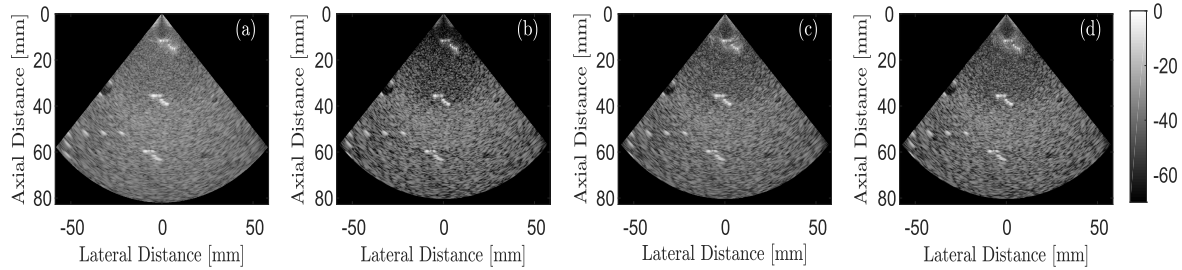

Fig. 13. Images of GAMMEX 404GSLE which include pin and resolution targets obtained with (a) DAS (63), (b) COBA (63), (c) SCOBA (21), and (d) SCOBAR (29). Number in brackets refers to the number of elements used.
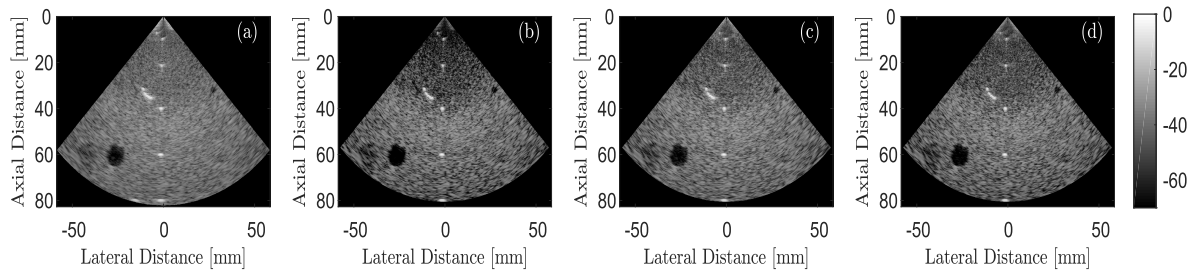

Fig. 14. Images of GAMMEX 403GSLE which include resolution and cystic targets obtained with (a) DAS (63), (b) COBA (63), (c) SCOBA (21), and (d) SCOBAR (29). Number in brackets refers to the number of elements used.
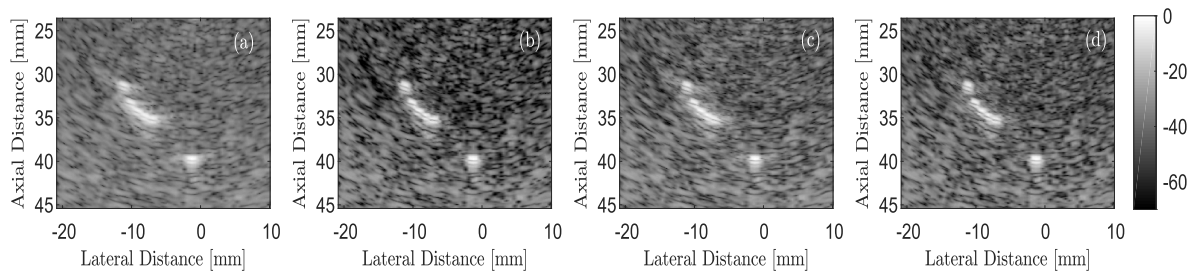

Fig. 15. Zoomed-in view on the resolution targets shown in Fig. 14.
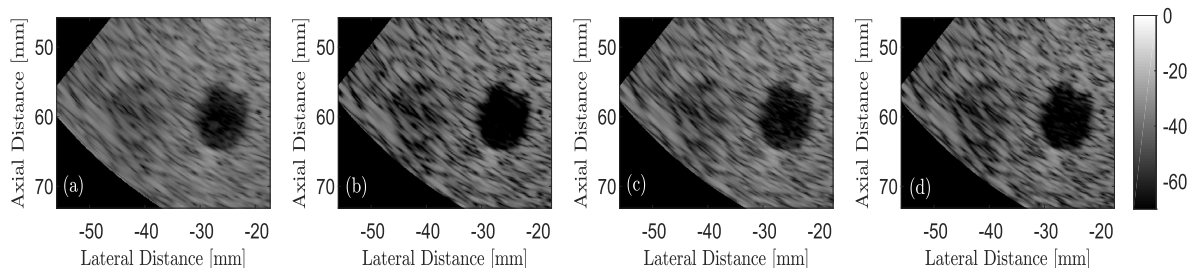

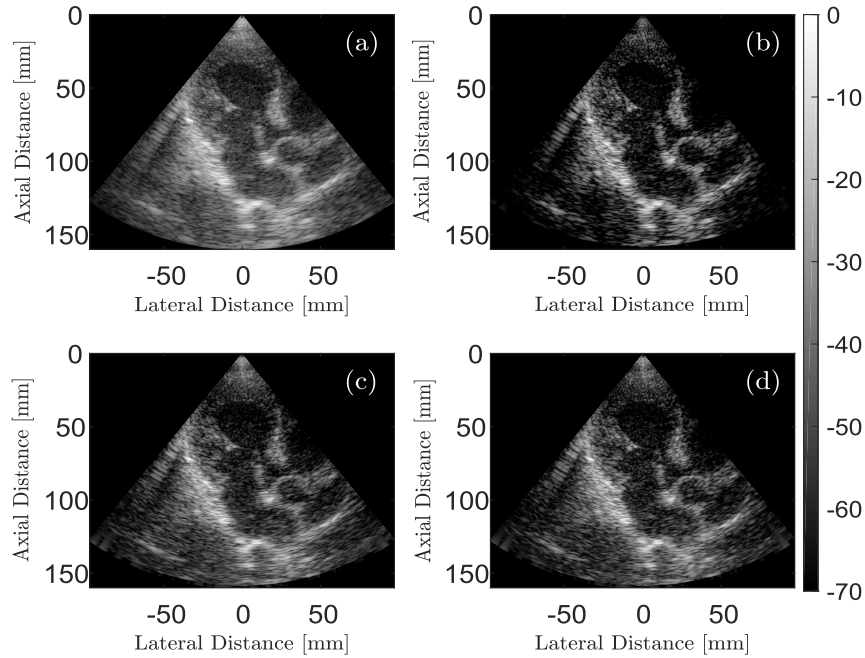Fig. 16. Zoomed-in view on the cystic targets displayed in Fig. 14.

Fig. 17. Cardiac images obtained with (a) DAS (63), (b) COBA (63), (c) SCOBA (21), and (d) SCOBAR (29). Number in brackets refers to the number of elements used.

-30.1 dB and the CR of SCOBA is similar and equal to -30 dB. The CR of SCOBAR and COBA is -34 and -44 dB, receptively. These results emphasize the superiority of COBA and demonstrate that a similar and improved performance to that of DAS can be obtained while using much fewer elements.

B. Phantom Scans

We next proceed to evaluate the proposed beamformers using experimental data. To that end, phantom data were acquired by a Verasonics Vantage 256 system. Tissue mimicking phantoms Gammex 403GSLE and 404GSLE were scanned by a 64-element phased array transducer P4-2v with a frequency response centered at 2.9 MHz and a sampling frequency of 11.9 MHz. The parameters for SCOBA and SCOBAR were chosen to be $A = 4$ and $B = 8$, resulting in 21 and 27 elements, respectively. The results obtained from different phantom scans are presented in Figs. 12–14 and include on-axis and off-axis targets, various cysts, and resolution target groups. Zoomed-in view on areas of cysts and resolution targets is shown in Figs. 15 and 16, respectively. As can be seen, COBA exhibits an improvement over DAS in terms of contrast and resolution, and SCOBA and SCOBAR achieve a similar performance to DAS and COBA, respectively, while using fewer elements.

C. In Vivo Acquisition

Finally, we apply the proposed methods on *in vivo* cardiac data. The acquisition was performed with a GE breadboard ultrasonic scanner where 63 acquisition channels were used. The radiated depth was 16 cm, the probe carrier frequency was 3.4 MHz, and the system sampling frequency was 16 MHz. For COBA, SCOBA, and SCOBAR, a Hanning window-based
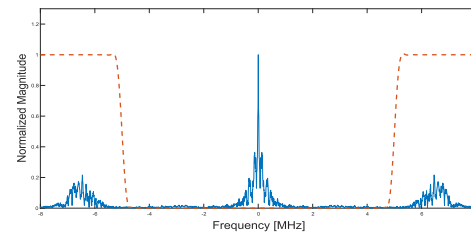

Fig. 18. Fourier transforms of the impulse response of the Hanning-based high-pass filter (dashed line) and the signal given by (21), which corresponds to the central *in vivo* image line.

high-pass filter was used (rather than a BP) with a cutoff frequency of 5 MHz, as shown in Fig. 18. The parameters for SCOBA and SCOBAR were set to $A = 4$ and $B = 8$, leading to the minimal numbers of elements that can be obtained as stated in Theorems 1 and 2. Consequently, 21 and 27 elements out of 63 were used by SCOBA and SCOBAR, respectively.

The results are presented in Fig. 17. Clearly, COBA outperforms DAS in terms of image quality; the background noise is reduced and the anatomical structures are better highlighted. SCOBA achieves a similar resolution as DAS, whereas SCOBAR yields notable resolution improvement. Moreover, both the sparse beamformers obtain a low noise floor compared with DAS, and thus, the heart walls are better defined. These results validate that using the proposed techniques, a reduction in the number of elements can be attained without compromising and even improving the image quality in comparison with the standard DAS.

VI. CONCLUSION

In this paper, we proposed three techniques for beamforming upon reception. First, we introduced a beamformer called

COBA, which is based on convolution of the RF signals and is implemented efficiently using FFT. Then, we introduced the concept of sum coarray to analyze the beam pattern generated by COBA, showing that it yields twofold enhancement in lateral resolution, compared with standard DAS, and provides contrast improvement. This was validated using qualitative and quantitative measurements in simulations, which emphasized that COBA leads to an increase in resolution, contrast, and noise suppression. In addition, an *in vivo* scan was provided for visual assessment of the resulting image quality.

Based on COBA and the sum coarray, we next presented two sparse beamformers, SCOBA and SCOBAR, which utilize a reduced number of elements. SCOBA requires much fewer elements without degrading image quality compared with DAS, whereas SCOBAR offers an improvement of resolution and contrast at the expense of a smaller, yet sizable, element reduction. The minimal number of elements in both algorithms is proportional to the square root of the number used with a full array. In addition, SCOBA may allow for a probe with a smaller physical aperture. The performance of SCOBA and SCOBAR was studied using both simulated and experimental data, verifying that only a small number of elements can be used while maintaining or improving the image quality compared with DAS. Images of *in vivo* cardiac scans demonstrate that SCOBA and SCOBAR are suitable for clinical use.

To conclude, the proposed methods provide a prominent improvement of contrast and lateral resolution in comparison with DAS. In addition, they allow for a significant element reduction while preserving or enhancing image quality. While the full aperture is required for transmission, most of receive electronics can be discarded using this approach. Thus, it enables the design of cheap, portable probes, and low-power ultrasound systems with a low computational load, paving the way to 3-D imaging and wireless operation.

APPENDIX A
DISCRETE CONVOLUTION

Consider two discrete sequences a and b of length $N+1$ and $M+1$, respectively. The discrete linear convolution of a and b is a sequence c of length $L = N+M+1$ whose entries are given by

$$c_s = \sum_{i=0}^{s} a_{s-i}b_i, \quad s = 0, 1, \ldots, L-1 \tag{72}$$

where a and b are zero padded to be of length L.

Let f and g be two polynomials defined by

$$f(p) = \sum_{n=0}^{N} a_n p^n, \quad g(p) = \sum_{m=0}^{M} b_m p^m. \tag{73}$$

Their product is

$$h(p) \triangleq f(p)g(p) = \sum_{n=0}^{N}\sum_{m=0}^{M} a_n b_m p^n p^m. \tag{74}$$

The latter can be viewed as a sum of single powers of p by substituting $s = n + m$

$$h(p) = \sum_{s=0}^{L-1} \left(\sum_{(n,m):\,n+m=s} a_n b_m \right) p^s. \tag{75}$$

The coefficients c_s of this polynomial are given by the inner summation, which can be expressed as

$$c_s = \sum_{(n,m):\,n+m=s} a_n b_m = \sum_{i=0}^{s} a_{s-i} b_s \tag{76}$$

where the second equality is obtained by zero padding a and b to be of length L. Thus, the coefficients of $h(p)$ are the linear convolution of a and b.

APPENDIX B
PROOF OF THEOREM 1

We consider the equivalent problem given by (57). It is clear from the constraints that A and B are both divisors of N and we can express B using A as $B = (N/A)$. Without loss of generality, we assume that $A \leq B$ that leads to the following formulation:

$$A^* = \arg\min_{m \in D_1} \; m + \frac{N}{m}. \tag{77}$$

Next, we define a function $g : [1, \sqrt{N}] \to \mathbb{R}^+$ over a continuous domain

$$g(x) = x + \frac{N}{x}.$$

The function $g(x)$ is continuous and differentiable over the open domain $(1, \sqrt{N})$. Its derivative is given by

$$\frac{dg}{dx} = 1 - \frac{N}{x^2} < 0$$

and hence, $g(x)$ is monotonically decreasing. Using the fact that $D_1 \subseteq [1, \sqrt{N}]$ and denoting $n = \max(D_1)$, it holds that

$$g(n) < g(m), \quad m \in D_1, \, m \neq n.$$

Therefore, the optimal solution is given by $A^* = n = \max(D_1)$ and $B^* = \min(D_2)$ accordingly. The solution for $B \leq A$ is established with the same arguments by interchanging the roles of A and B. □

Notice that when N is a perfect square, we have that $\max(D_1) = \min(D_2)$, leading to the single solution described earlier. In general, there are two optimal solutions; however, the solution in which $B \geq A$ is superior to the second one in terms of mutual coupling.

APPENDIX C
PROOF OF THEOREM 2

We consider the equivalent problem (65). Denoting $M = 2A \in \mathbb{E}$, we rewrite it as

$$M^*, B^* = \arg\min_{M, B \in \mathbb{N}, \, B > 1} \; M + B$$
$$\text{s.t. } MB = 2N$$
$$M \in \mathbb{E}. \tag{78}$$

Ignoring for a moment the last constraint, problem (78) is similar to (57) with $2N$ replacing N. Hence, by similar arguments to those presented in the proof of Theorem 1, we have that

$$M^* = \max(D_3) \quad \text{and} \quad B^* = \min(D_4)$$
$$M^* = \min(D_4) \quad \text{and} \quad B^* = \max(D_3). \tag{79}$$

Now, we enforce the constraint $M \in \mathbb{E}$. Since $\max(D_3)\min(D_4) = 2N$ either $\max(D_3)$ or $\min(D_4)$ are even, or both, therefore, at least one of the optimal solutions in (79) is valid. Thus, taking into account that $A^* = M^*/2$, we get the optimal solutions presented for each one of the three cases. $\square$

Notice that when $2N$ is a perfect square, we have that $\max(D_3) = \min(D_4) = \sqrt{2N} \in \mathbb{E}$ and the solution is $A = \sqrt{(N/2)}$, $B = \sqrt{2N}$, as presented before.

REFERENCES

[1] K. E. Thomenius, "Evolution of ultrasound beamformers," in *Proc. IEEE Ultrason. Symp.*, vol. 2, Nov. 1996, pp. 1615–1622.

[2] K. Ranganathan and W. F. Walker, "A novel beamformer design method for medical ultrasound. Part I: Theory," *IEEE Trans. Ultrason., Ferroelectr., Freq. Control*, vol. 50, no. 1, pp. 15–24, Jan. 2003.

[3] M. Karaman, P.-C. Li, and M. O'Donnell, "Synthetic aperture imaging for small scale systems," *IEEE Trans. Ultrason., Ferroelectr., Freq. Control*, vol. 42, no. 3, pp. 429–442, May 1995.

[4] J. A. Jensen, S. I. Nikolov, K. L. Gammelmark, and M. H. Pedersen, "Synthetic aperture ultrasound imaging," *Ultrasonics*, vol. 44, p. e5, Dec. 2006.

[5] G. R. Lockwood, J. R. Talman, and S. S. Brunke, "Real-time 3-D ultrasound imaging using sparse synthetic aperture beamforming," *IEEE Trans. Ultrason., Ferroelectr., Freq. Control*, vol. 45, no. 4, pp. 980–988, Jul. 1998.

[6] B. Van Veen and K. Buckley, "Beamforming techniques for spatial filtering," in *Digital Signal Processing Handbook*. Boca Raton, FL, USA: CRC Press, 1997, pp. 1–61.

[7] F. Viola and W. F. Walker, "Adaptive signal processing in medical ultrasound beamforming," in *Proc. IEEE Ultrason. Symp.*, vol. 4, Sep. 2005, pp. 1980–1983.

[8] W. Chen, Y. Zhao, and J. Gao, "Improved Capon Beamforming Algorithm by using inverse covariance matrix calculation," in *Proc. IET Int. Radar Conf.*, Apr. 2013, pp. 1–6.

[9] K. Kim, S. Park, J. Kim, S.-B. Park, and M. Bae, "A fast minimum variance beamforming method using principal component analysis," *IEEE Trans. Ultrason., Ferroelectr., Freq. Control*, vol. 61, no. 6, pp. 930–945, Jun. 2014.

[10] J. F. Synnevag, A. Austeng, and S. Holm, "Adaptive beamforming applied to medical ultrasound imaging," *IEEE Trans. Ultrason., Ferroelectr., Freq. Control*, vol. 54, no. 8, pp. 1606–1613, Aug. 2007.

[11] B. M. Asl and A. Mahloojifar, "Minimum variance beamforming combined with adaptive coherence weighting applied to medical ultrasound imaging," *IEEE Trans. Ultrason., Ferroelectr., Freq. Control*, vol. 56, no. 9, pp. 1923–1931, Sep. 2009.

[12] C.-I. Nilsen and I. Hafizovic, "Beamspace adaptive beamforming for ultrasound imaging," *IEEE Trans. Ultrason., Ferroelectr., Freq. Control*, vol. 56, no. 10, pp. 2187–2197, Oct. 2009.

[13] A. C. Jensen and A. Austeng, "An approach to multibeam covariance matrices for adaptive beamforming in ultrasonography," *IEEE Trans. Ultrason., Ferroelectr., Freq. Control*, vol. 59, no. 6, pp. 1139–1148, Jun. 2012.

[14] A. C. Jensen and A. Austeng, "The iterative adaptive approach in medical ultrasound imaging," *IEEE Trans. Ultrason., Ferroelectr., Freq. Control*, vol. 61, no. 10, pp. 1688–1697, Oct. 2014.

[15] T. Yardibi, J. Li, and P. Stoica, "Nonparametric and sparse signal representations in array processing via iterative adaptive approaches," in *Proc. 42nd Asilomar Conf. Signals, Syst. Comput.*, Oct. 2008, pp. 278–282.

[16] D. A. Guenther and W. F. Walker, "Robust finite impulse response beamforming applied to medical ultrasound," *IEEE Trans. Ultrason., Ferroelectr., Freq. Control*, vol. 56, no. 6, pp. 1168–1188, Jun. 2009.

[17] M. A. Lediju, G. E. Trahey, B. C. Byram, and J. J. Dahl, "Short-lag spatial coherence of backscattered echoes: Imaging characteristics," *IEEE Trans. Ultrason., Ferroelectr., Freq. Control*, vol. 58, no. 7, pp. 1377–1388, Jul. 2011.

[18] J. J. Dahl, D. Hyun, M. Lediju, and G. E. Trahey, "Lesion detectability in diagnostic ultrasound with short-lag spatial coherence imaging," *Ultrason. Imag.*, vol. 33, no. 2, pp. 119–133, Apr. 2011.

[19] G. Matrone, A. S. Savoia, G. Caliano, and G. Magenes, "The delay multiply and sum beamforming algorithm in ultrasound B-mode medical imaging," *IEEE Trans. Med. Imag.*, vol. 34, no. 4, pp. 940–949, Apr. 2015.

[20] G. Matrone, A. Ramalli, A. S. Savoia, P. Tortoli, and G. Magenes, "High frame-rate, high resolution ultrasound imaging with multi-line transmission and filtered-delay multiply and sum beamforming," *IEEE Trans. Med. Imag.*, vol. 36, no. 2, pp. 478–486, Feb. 2017.

[21] G. Matrone, A. S. Savoia, G. Caliano, and G. Magenes, "Depth-of-field enhancement in filtered-delay multiply and sum beamformed images using synthetic aperture focusing," *Ultrasonics*, vol. 75, pp. 216–225, Mar. 2017.

[22] G. Matrone, A. S. Savoia, G. Caliano, and G. Magenes, "Ultrasound synthetic aperture focusing with the delay multiply and sum beamforming algorithm," in *Proc. 37th Annu. Int. Conf. Eng. Med. Biol. Soc. (EMBC)*, Aug. 2015, pp. 137–140.

[23] G. Matrone, A. S. Savoia, G. Caliano, and G. Magenes, "Ultrasound plane-wave imaging with delay multiply and sum beamforming and coherent compounding," in *Proc. 38th Annu. Int. Conf. Eng. Med. Biol. Soc. (EMBC)*, Aug. 2016, pp. 3223–3226.

[24] G. Matrone, A. Ramalli, P. Tortoli, and G. Magenes, "Experimental evaluation of ultrasound higher-order harmonic imaging with Filtered-Delay Multiply And Sum (F-DMAS) non-linear beamforming," *Ultrasonics*, vol. 86, pp. 59–68, May 2018.

[25] M. Mozaffarzadeh, M. Sadeghi, A. Mahloojifar, and M. Orooji, "Double-stage delay multiply and sum beamforming algorithm applied to ultrasound medical imaging," *Ultrasound Med. Biol.*, vol. 44, no. 3, pp. 677–686, Mar. 2017.

[26] Y. C. Eldar and G. Kutyniok, *Compressed Sensing: Theory and Applications*. Cambridge, U.K.: Cambridge Univ. Press, 2012.

[27] Y. C. Eldar, *Sampling Theory: Beyond Bandlimited Systems*. Cambridge, U.K.: Cambridge Univ. Press, 2015.

[28] N. Wagner, Y. C. Eldar, and Z. Friedman, "Compressed beamforming in ultrasound imaging," *IEEE Trans. Signal Process.*, vol. 60, no. 9, pp. 4643–4657, Sep. 2012.

[29] T. Chernyakova and Y. Eldar, "Fourier-domain beamforming: The path to compressed ultrasound imaging," *IEEE Trans. Ultrason., Ferroelectr., Freq. Control*, vol. 61, no. 8, pp. 1252–1267, Aug. 2014.

[30] T. Chernyakova *et al.*, "Fourier-domain beamforming and structure-based reconstruction for plane-wave imaging," *IEEE Trans. Ultrason., Ferroelectr., Freq. Control*, vol. 65, no. 10, pp. 1810–1821, Oct. 2018.

[31] H. Liebgott, R. Prost, and D. Friboulet, "Pre-beamformed RF signal reconstruction in medical ultrasound using compressive sensing," *Ultrasonics*, vol. 53, pp. 525–533, Feb. 2013.

[32] J. Liu, Q. He, and J. Luo, "A compressed sensing strategy for synthetic transmit aperture ultrasound imaging," *IEEE Trans. Med. Imag.*, vol. 36, no. 4, pp. 878–891, Apr. 2017.

[33] J. D. Larson, III, "2-D phased array ultrasound imaging system with distributed phasing," U.S. Patent 5 229 933, Nov. 11, 1993.

[34] B. Savord and R. Solomon, "Fully sampled matrix transducer for real time 3D ultrasonic imaging," in *Proc. IEEE Symp. Ultrason.*, vol. 1. Oct. 2003, pp. 945–953.

[35] M. I. Fuller, E. V. Brush, M. D. C. Eames, T. N. Blalock, J. A. Hossack, and W. F. Walker, "The sonic window: Second generation prototype of low-cost, fully-integrated, pocket-sized medical ultrasound device," in *Proc. IEEE Ultrason. Symp.*, vol. 1, Sep. 2005, pp. 273–276.

[36] W. Lee, S. F. Idriss, P. D. Wolf, and S. W. Smith, "A miniaturized catheter 2-D array for real-time, 3-D intracardiac echocardiography," *IEEE Trans. Ultrason., Ferroelectr., Freq. Control*, vol. 51, no. 10, pp. 1334–1346, Oct. 2004.

[37] R. E. Davidsen, J. A. Jensen, and S. W. Smith, "Two-dimensional random arrays for real time volumetric imaging," *Ultrason. Imag.*, vol. 16, no. 3, pp. 143–163, 1994.

[38] S. S. Brunke and G. R. Lockwood, "Broad-bandwidth radiation patterns of sparse two-dimensional vernier arrays," *IEEE Trans. Ultrason., Ferroelectr., Freq. Control*, vol. 44, no. 5, pp. 1101–1109, Sep. 1997.

[39] J. T. Yen, J. P. Steinberg, and S. W. Smith, "Sparse 2-D array design for real time rectilinear volumetric imaging," *IEEE Trans. Ultrason., Ferroelectr., Freq. Control*, vol. 47, no. 1, pp. 93–110, Jan. 2000.

[40] A. Austeng and S. Holm, "Sparse 2-D arrays for 3-D phased array imaging—Design methods," *IEEE Trans. Ultrason., Ferroelectr., Freq. Control*, vol. 49, no. 8, pp. 1073–1086, Aug. 2002.

[41] M. Karaman, I. O. Wygant, Ö. Oralkan, and B. T. Khuri-Yakub, "Minimally redundant 2-D array designs for 3-D medical ultrasound imaging," *IEEE Trans. Med. Imag.*, vol. 28, no. 7, pp. 1051–1061, Jul. 2009.

[42] B. Diarra, M. Robini, P. Tortoli, C. Cachard, and H. Liebgott, "Design of optimal 2-D nongrid sparse arrays for medical ultrasound," *IEEE Trans. Biomed. Eng.*, vol. 60, no. 11, pp. 3093–3102, Nov. 2013.

[43] S. Ramadas, J. C. Jackson, J. Dziewierz, R. O'Leary, and A. Gachagan, "Application of conformal map theory for design of 2-D ultrasonic array structure for NDT imaging application: A feasibility study," *IEEE Trans. Ultrason., Ferroelectr., Freq. Control*, vol. 61, no. 3, pp. 496–504, Mar. 2014.

[44] E. Roux *et al.*, "Validation of optimal 2D sparse arrays in focused mode: Phantom experiments," in *Proc. IEEE Int. Ultrason. Symp. (IUS)*, Sep. 2017, pp. 1–4.

[45] S. K. Mitra, K. Mondal, M. K. Tchobanou, and G. Jovanovic, "General polynomial factorization-based design of sparse periodic linear arrays," *IEEE Trans. Ultrason., Ferroelectr., Freq. Control*, vol. 57, no. 9, pp. 1952–1966, Sep. 2010.

[46] A. I. H. Chen, L. L. Wong, A. S. Logan, and J. T. W. Yeow, "A CMUT-based real-time volumetric ultrasound imaging system with row-column addressing," in *Proc. IEEE Int. Ultrason. Symp. (IUS)*, Oct. 2011, pp. 1755–1758.

[47] M. F. Rasmussen and J. A. Jensen, "3D ultrasound imaging performance of a row–column addressed 2D array transducer: A simulation study," in *Proc. SPIE Med. Imag.*, 2013, Art. no. 86750C.

[48] M. F. Rasmussen and J. A. Jensen, "3-D ultrasound imaging performance of a row-column addressed 2-D array transducer: A measurement study," in *Proc. Int. Ultrason. Symp. (IUS)*, Jul. 2013, pp. 1460–1463.

[49] M. F. Rasmussen, T. L. Christiansen, E. V. Thomsen, and J. A. Jensen, "3-D imaging using row-column-addressed arrays with integrated apodization—Part I: Apodization design and line element beamforming," *IEEE Trans. Ultrason., Ferroelectr., Freq. Control*, vol. 62, no. 5, pp. 947–958, May 2015.

[50] T. L. Christiansen, M. F. Rasmussen, J. P. Bagge, L. N. Moesner, J. A. Jensen, and E. V. Thomsen, "3-D imaging using row–column-addressed arrays with integrated apodization—Part II: Transducer fabrication and experimental results," *IEEE Trans. Ultrason., Ferroelectr., Freq. Control*, vol. 62, no. 5, pp. 959–971, May 2015.

[51] R. Cohen and Y. C. Eldar, "Optimized sparse array design based on the sum coarray," in *Proc. Int. Conf. Acoust., Speech Signal Process. (ICASSP)*, Apr. 2018, pp. 3340–3343.

[52] R. T. Hoctor and S. A. Kassam, "The unifying role of the coarray in aperture synthesis for coherent and incoherent imaging," *Proc. IEEE*, vol. 78, no. 4, pp. 735–752, Apr. 1990.

[53] J. A. Jensen, "Linear description of ultrasound imaging systems," Notes Int. Summer School Adv. Ultrasound Imag., Dept. Elect. Eng., Tech. Univ. Denmark, Lyngby, Denmark, Jul. 1999.

[54] J. Park, S. Jeon, J. Meng, L. Song, J. S. Lee, and C. Kim, "Delay-multiply-and-sum-based synthetic aperture focusing in photoacoustic microscopy," *J. Biomed. Opt.*, vol. 21, no. 3, p. 036010, 2016.

[55] T. Su, D. Li, and S. Zhang, "An efficient subarray average delay multiply and sum beamformer algorithm in ultrasound imaging," *Ultrasonics*, vol. 84, pp. 411–420, Mar. 2018.

[56] P. Pal and P. P. Vaidyanathan, "Nested arrays: A novel approach to array processing with enhanced degrees of freedom," *IEEE Trans. Signal Process.*, vol. 58, no. 8, pp. 4167–4181, Aug. 2010.

[57] M. I. Skolnik, *Introduction to Radar Systems*. New York, NY, USA: McGraw-Hill, 2001.

[58] C.-L. Liu and P. P. Vaidyanathan, "Super nested arrays: Sparse arrays with less mutual coupling than nested arrays," in *Proc. Int. Conf. Acoust., Speech Signal Process. (ICASSP)*, Mar. 2016, pp. 2976–2980.

[59] C.-L. Liu and P. P. Vaidyanathan, "Super nested arrays: Linear sparse arrays with reduced mutual coupling—Part I: Fundamentals," *IEEE Trans. Signal Process.*, vol. 64, no. 15, pp. 3997–4012, Aug. 2016.

[60] C.-L. Liu and P. P. Vaidyanathan, "Super nested arrays: Linear sparse arrays with reduced mutual coupling—Part II: High-order extensions," *IEEE Trans. Signal Process.*, vol. 64, no. 16, pp. 4203–4217, Aug. 2016.

[61] A. Fenster and J. C. Lacefield, *Ultrasound Imaging and Therapy*. Boca Raton, FL, USA: CRC Press, 2015.

[62] J. A. Jensen, "Field: A program for simulating ultrasound systems," in *Proc. 10th Nordicbaltic Conf. Biomed. Imag.*, vol. 4, 1996, pp. 351–353.

[63] J. A. Jensen and N. B. Svendsen, "Calculation of pressure fields from arbitrarily shaped, apodized, and excited ultrasound transducers," *IEEE Trans. Ultrason., Ferroelectr., Freq. Control*, vol. 39, no. 2, pp. 262–267, Mar. 1992.

[64] T. Chernyakova, D. Cohen, M. Shoham, and Y. C. Eldar. (2018). "iMAP beamforming for high quality high frame rate imaging." [Online]. Available: https://arxiv.org/abs/1806.03526

Regev Cohen (GS'16) received the B.Sc. degree *(summa cum laude)* in electrical engineering from the Technion–Israel Institute of Technology, Haifa, Israel, in 2015, where he is currently pursuing the Ph.D. degree in electrical engineering.

His research interests include theoretical aspects of signal processing, sampling theory, compressed sensing, optimization methods, sparse array design, deep learning, and advanced signal processing methods for ultrasonic imaging.

Mr. Cohen received the Meyer Foundation Excellence Award and Elias-Perlmutter Award in 2015. In 2017, he received the Israel and Debora Cederbaum Scholarship.

Yonina C. Eldar (S'98–M'02–SM'07–F'12) received the B.Sc. degree in physics and the B.Sc. degree in electrical engineering from Tel Aviv University, Tel Aviv, Israel, in 1995 and 1996, respectively, and the Ph.D. degree in electrical engineering and computer science from the Massachusetts Institute of Technology (MIT), Cambridge, MA, USA, in 2002.

She was a Visiting Professor at Stanford University, Stanford, CA, USA. She is currently a Professor with the Department of Electrical Engineering, Technion–Israel Institute of Technology, Haifa, Israel, where she holds the Edwards Chair in engineering. She is also a Research Affiliate with the Research Laboratory of Electronics, MIT, and an Adjunct Professor at Duke University, Durham, NC, USA. She has authored the book *Sampling Theory: Beyond Bandlimited Systems* and co-authored the books *Compressed Sensing* (Cambridge University Press) and *Convex Optimization Methods in Signal Processing and Communications* (Cambridge University Press). Her research interests include the broad areas of statistical signal processing, sampling theory and compressed sensing, optimization methods, and their applications to biology and optics.

Dr. Eldar was a member of the Young Israel Academy of Science and Humanities, the Israel Committee for Higher Education, the IEEE Signal Processing Theory and Methods, and Bio Imaging Signal Processing Technical Committees. She is a member of the Israel Academy of Sciences and Humanities (elected in 2017) and the IEEE Sensor Array and Multichannel Technical Committee. She was a Horev Fellow of the Leaders in Science and Technology Program at the Technion–Israel Institute of Technology and an Alon fellow. She is a EURASIP Fellow. She has received many awards for excellence in research and teaching, including the IEEE Signal Processing Society Technical Achievement Award in 2013, the IEEE/AESS Fred Nathanson Memorial Radar Award in 2014, and the IEEE Kiyo Tomiyasu Award in 2016. She received the Michael Bruno Memorial Award from the Rothschild Foundation, the Weizmann Prize for Exact Sciences, the Wolf Foundation Krill Prize for Excellence in Scientific Research, the Henry Taub Prize for Excellence in Research (twice), the Hershel Rich Innovation Award (three times), the Award for Women with Distinguished Contributions, the Andre and Bella Meyer Lectureship, the Career Development Chair at the Technion–Israel Institute of Technology, the Muriel & David Jacknow Award for Excellence in Teaching, and the Technion's Award for Excellence in Teaching (two times). She received several best paper awards and best demo awards together with her research students and colleagues, including the SIAM Outstanding Paper Prize, the UFFC Outstanding Paper Award, the Signal Processing Society Best Paper Award, and the IET Circuits, Devices and Systems Premium Award. She was selected as one of the 50 most influential women in Israel. She was a co-chair and a technical co-chair of several international conferences and workshops. She was a Signal Processing Society Distinguished Lecturer. She served as an Associate Editor for the IEEE TRANSACTIONS ON SIGNAL PROCESSING, the *EURASIP Journal of Signal Processing*, the *SIAM Journal on Matrix Analysis and Applications*, and the *SIAM Journal on Imaging Sciences*. She is the Editor-in-Chief of *Foundations and Trends in Signal Processing* and serves on several other IEEE committees.